Short Papers

Arbitrarily Oriented Perfectly Matched Layer in the Frequency Domain

Xiaoming Xu and Robin Sloan

***Abstract*—An arbitrarily oriented perfectly matched layer (PML) is introduced by using complex space mapping for more flexible meshing of microwave engineering problems. The PML can be oriented in any direction. The discussion is extended to two-direction PML's for matching the interface between one-direction PML's, and three-direction PML's for two-direction ones. An example having analytical solution is calculated. Numerical results agree with the analytical solution very well within 0.1%.**

***Index Terms*—Absorbing boundary, finite element, perfectly matched layer.**

I. Introduction

Berenger [1] introduced a nonphysical medium, i.e., the perfectly matched layer (PML), for absorbing propagating electromagnetic waves. It has been noticed that most of the theoretical discussion and applications are limited to the orthodox PML structure oriented along Cartesian coordinate axes. To remove this limitation from practical PML structures, especially for flexible finite-element meshing, arbitrarily oriented PML's are introduced by the authors. The facets of this kind of PML are still planes, but they can be oriented in any direction without limitation, as shown in Fig. 1. This characteristic provides more flexibility to construct PML structures fitting the complex geometry of engineering problems.

II. Formulation

The nonphysical electromagnetic characteristics of a PML are described mathematically. In the frequency domain, PML equations can be represented by anisotropic complex mapping. Using the mapping method introduced by Rappaport [2], [3], the mapping carried out along normal directions of interfaces between free space and PML's can lead to an useful formulation [4], in which the whole set of equations for the PML keeps the conventional form, except the normal mapping is applied to space coordinate systems. Maxwell's equations are generalized for the PML as follows:

$$\nabla_g \times \mathbf{H} = j\omega\mathbf{D}$$
$$\nabla_g \times \mathbf{E} = -j\omega\mathbf{B}$$
$$\nabla_g \cdot \mathbf{D} = 0$$
$$\nabla_g \cdot \mathbf{B} = 0$$

where ∇_g is a differential operator, similar to ∇' used by other researchers working on PML's. The subscript $_g$ declares that the operator is defined in a generalized coordinate system and also indicates the number of mapping directions. $g = 0$ means that no mapping is applied in conventional materials, and $g = 1, 2, 3$ means that one, two, and three coordinates are scaled in a one-, two- and three-direction-oriented PML, respectively.

Manuscript received August 27, 1998; revised December 10, 1999. This work was supported in part by the Engineering and Physical Sciences Research Council under Contract GR/K78744.

The authors are with the Department of Electrical Engineering and Electronics, University of Manchester Institute of Science and Technology, Manchester M60 1QD U.K. (e-mail: xu@ae.ee.umist.ac.uk).

Publisher Item Identifier S 0018-9480(00)02059-7.

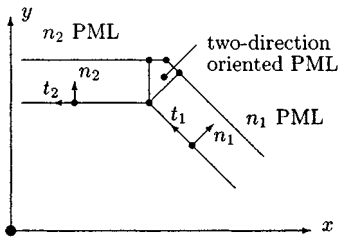

Fig. 1. Two-dimensional display of arbitrarily oriented PML's.

A. Mapping Along Rotated Coordinates

Rotated rectangular coordinate systems are used for various orientations of PML's. The n-axis indicates the normal direction of the interface between the free space and a one-direction-oriented PML. Also, the t and τ are the first and second tangential axes, respectively.

Complex mapping is carried out along the rotated coordinate axes to produce a complex coordinate system for the PML as follows:

$$\frac{\partial n'}{\partial n} = s_n \quad \frac{\partial t'}{\partial t} = s_t \quad \frac{\partial \tau'}{\partial \tau} = s_\tau. \tag{1}$$

The mapping scales s_m $(m = n, t, \tau)$ are complex parameters with a unit real part and negative imaginary part. When the imaginary part is set equal to zero, the scale $s_m = 1$ then denotes that no mapping is applied along the m-direction.

Partial derivatives along the mapped coordinates are read in a matrix form

$$\left[\frac{\partial}{\partial n', t', \tau'}\right] = [J_m]\left[\frac{\partial}{\partial n, t, \tau}\right] \tag{2}$$

where the Jacobean matrix for mapping $[J_m]$ is diagonal as follows:

$$[J_m] = \operatorname{diag}\left[\frac{\partial n}{\partial n'}, \frac{\partial t}{\partial t'}, \frac{\partial \tau}{\partial \tau'}\right] = \operatorname{diag}\left[\frac{1}{s_n}, \frac{1}{s_t}, \frac{1}{s_\tau}\right]. \tag{3}$$

B. Transformation Between Coordinate Systems

In three-dimensional space, a transformation of coordinate rotation from the x–y–z system to the $n - t - \tau$ system is expressed as

$$\begin{bmatrix} n \\ t \\ \tau \end{bmatrix} = \begin{bmatrix} n_x & n_y & n_z \\ t_x & t_y & t_z \\ \tau_x & \tau_y & \tau_z \end{bmatrix} \begin{bmatrix} x \\ y \\ z \end{bmatrix} = [R] \begin{bmatrix} x \\ y \\ z \end{bmatrix}. \tag{4}$$

The items in the rotation matrix $[R]$ are components of the unit vectors, which can be defined by the cosine of the angle between the relevant coordinate axes, such as $n_x = \cos(n, x)$.

Also, the unit vectors along the rotated coordinate axes $n - t - \tau$ can be represented by components in Cartesian coordinates as

$$[\hat{n}, \hat{t}, \hat{\tau}]^T = [R][\hat{x}, \hat{y}, \hat{z}]^T. \tag{5}$$

The transformation of partial derivatives reads as

$$\left[\frac{\partial}{\partial n, t, \tau}\right] = [J_r]\left[\frac{\partial}{\partial x, y, z}\right] \tag{6}$$

where J_r signifies the Jacobean matrix for coordinate rotation. Obviously, the Jacobean matrix is equal to the rotation matrix

$$[J_r] = \left[\frac{\partial x, y, x}{\partial n, t, \tau}\right] = \left[[R]^{-1}\right]^T = \left[[R]^T\right]^T = [R]. \tag{7}$$

C. Generalized Operator

The generalized operator for a PML is defined in the mapped coordinate system, then converted to the rotated coordinates, and finally, is reversed to Cartesian coordinates, which are the common coordinates for various PML's

$$\nabla_g = \hat{n}\frac{\partial}{\partial n'} + \hat{t}\frac{\partial}{\partial t'} + \hat{\tau}\frac{\partial}{\partial \tau'} = [\hat{x}, \hat{y}, \hat{z}]^T [D] \left[\frac{\partial}{\partial x, y, z}\right] \tag{8}$$

where the whole transformation matrix for derivatives $[D]$ includes the operations of coordinate rotation and complex mapping for the PML

$$[D] = [R]^T [J_m][J_r] = [d_{ij}] \tag{9}$$

$$d_{ij} = \frac{n_i n_j}{s_n} + \frac{t_i t_j}{s_t} + \frac{\tau_i \tau_j}{s_\tau} \tag{10}$$

where $i, j = x, y, z$.

III. Design of PML Structure

Similar to an orthodox structure, one-direction PML plates are used to enclose a calculation domain. However, their orientations are no longer limited along Cartesian coordinates. At an edge between two one-direction PML plates, a two-direction PML is needed to buffer the one-direction PML's because they cannot match each other. Similarly, on corners, three-direction PML's are used.

A. One-Direction-Oriented PML

In a one-direction-oriented PML, the mapping is applied only along its n-direction. Therefore, the mapping scales along t- and τ-directions should be set unity $s_t = s_\tau = 1$. Considering the following identical equation:

$$n_i n_j + t_i t_j + \tau_i \tau_j = \delta_{ij} = \begin{cases} 1, & \text{when } i = j \\ 0, & \text{when } i \neq j \end{cases} \tag{11}$$

(10) then reduces to

$$d_{ij}^n = \delta_{ij} + \left(\frac{1}{s_n} - 1\right) n_i n_j. \tag{12}$$

B. Two-Direction-Oriented PML

Similar to the installation of a compatible orthodox PML structure, two-direction-oriented PML's are used at the edges. When setting the mapping scale along the third direction τ equal to unity, $s_\tau = 1$, (10) becomes

$$d_{ij}^{nt} = \frac{n_i n_j}{s_n} + \frac{t_i t_j}{s_t} + \tau_i \tau_j \tag{13}$$

but the design of mapping scales for the two-direction-oriented PML becomes more complex this time. On the interface surface to the first one-direction PML, the two-direction PML should fit to the interfacing PML oriented in the n_1 direction. That means the mapping scale of the two-direction PML along the n_1 direction must be identical to the corresponding one for the one-direction PML. Also, on the second interface, it should fit to another one-direction PML.

In general, the orientations of the neighboring arbitrarily oriented PML's will not be perpendicular to each other. Therefore, care must be taken setting the mapping scales. Fortunately, there is an easy solution, when a common mapping scale is applied to the relevant PML's.

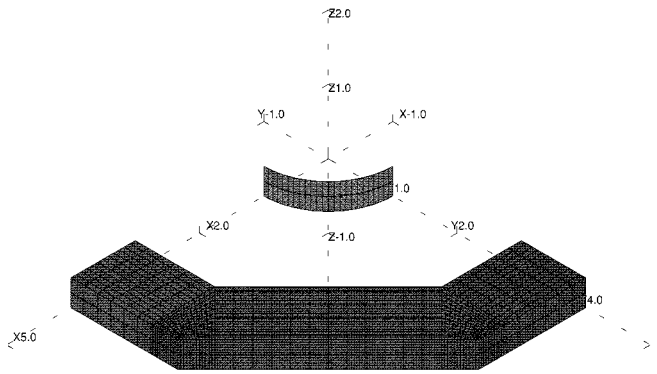

Fig. 2. Arbitrarily oriented PML's and inner boundary surface.

Considering a two-direction PML having a common mapping scale for both n- and t-directions, $s_n = s_t = s_c$. After substituting (11), (13) becomes

$$d_{ij}^{nt}(s_n = s_t = s_c) = \frac{\delta_{ij}}{s_c} + \left(1 - \frac{1}{s_c}\right)\tau_i \tau_j. \tag{14}$$

The above equation implies that all co-plane two-direction PML's are equivalent to each other, when a common mapping scale is applied to both PML's. Therefore, by applying the common mapping scale to two neighboring one-direction PML's and the buffering two-direction PML, the relevant interfacing PML's are matched to each other.

C. Three-Direction-Oriented PML

On corners, three-direction PML's are needed, and complex mapping is carried out along three directions.

In practice, a common mapping scale is applied for convenient matching. Obviously, (10) reduces to

$$d_{ij}^{nt\tau}(s_n = s_t = s_\tau = s_c) = \frac{n_i n_j + t_i t_j + \tau_i \tau_j}{s_c} = \frac{\delta_{ij}}{s_c}. \tag{15}$$

This means all three-direction PML's having a common scale are equivalent to the x–y–z PML

$$\nabla_3(s_n = s_t = s_\tau = s_c) = \hat{x}\frac{1}{s_c}\frac{\partial}{\partial x} + \hat{y}\frac{1}{s_c}\frac{\partial}{\partial y} + \hat{z}\frac{1}{s_c}\frac{\partial}{\partial z}. \tag{16}$$

D. Common Mapping Scale for Compatible Structure

Therefore, application of a common mapping scale to a PML structure consisting of one-, two- and three-direction PML's will make easy matching between interfacing PML's.

IV. Numerical Example

Electromagnetic fields around a straight current line along the z-axis are calculated to verify the formulation for the arbitrarily oriented PML. The electric field has only an axial component with respect to one variable. The magnetic vector potential $\mathbf{A}$ is read as

$$A_z = A_0 H_0^{(2)}(k_0 r) \tag{17}$$

where $H_0^{(2)}$ is the Hankel function of the second kind with the lowest order. A_0 is chosen to let $A_z = 1$ on a boundary at $r = 1.0$ cm in the following finite-element calculation.

To save computational costs, only the sector between x- and y-axes is meshed. The field source of the current line is modeled by a Dirichlet condition on the inner boundary of the mesh at $r = 1.0$ cm. Three blocks of the one-direction-oriented PML constitute the PML wall interfacing free space. They are oriented along the x, y, and diagonal directions. Two wedges of two-direction-oriented PML are used as

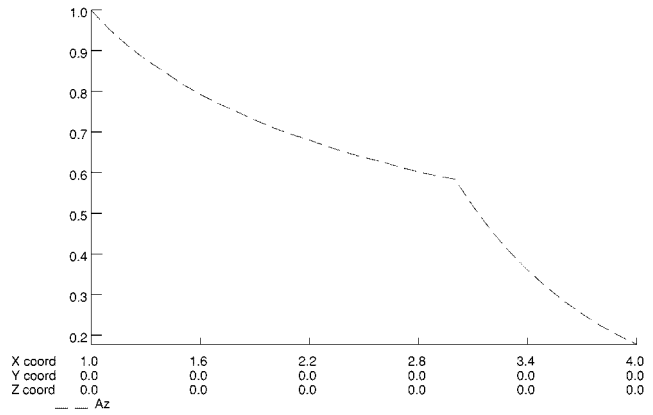

Fig. 3. FE result: A_z along x-axis arbitrarily oriented PML.

buffers between one-direction PML's of different orientations. The PML structure is placed about 2.0 cm away from the inner boundary ($x, y = 3.0$ cm on coordinate axes), as shown in Fig. 2. The required thickness of the PML depends on the frequency and mapping scale, which both determine the absorbing rate. In the numerical example, the main absorption is provided by the PML structure having thickness of 1.0 cm and mapping scale $s = 1 - j0.5$ at $f = 10$ GHz.

Along the thickness, 12 linear finite elements are evenly installed to model a decaying waveform. The area of free space is covered by 25 elements along the propagating direction from 1.0 to 3.0 cm and 24 elements along the arc between x- and y-axes.

The distribution of the magnetic vector potential calculated by the finite-element method is displayed along the x-axis in Fig. 3. Along the radial direction, A_z decays faster within the PML owing to absorption of the artificial material. Comparison between the finite-element result and the analytical solution was carried out for the domain between the inner boundary and PML walls. Very good agreement is achieved with an error range of less than 0.1%.

V. Conclusion

Electromagnetic equations for arbitrarily oriented PML's are introduced using the complex space mapping method. The configuration of a matched PML structure of arbitrarily oriented PML's is discussed. A simple example having an analytical solution is calculated for comparison. Good agreement within 0.1% between the numerical result and analytical solution shows that the radiation wave is absorbed by the PML absorber.

Acknowledgment

The authors would like to thank Dr. C. R. I. Emson and Prof. Trowbridge, Vector Fields Ltd., Oxford, U.K., for their help.

References

[1] J.-P. Berenger, "A perfectly matched layer for the absorption of electromagnetic wave," *J. Comput. Phys.*, vol. 114, pp. 185–200, 1994.

[2] C. M. Rappaport, "Perfectly matched absorbing boundary conditions based on anisotropic lossy mapping of space," *IEEE Microwave Guided Wave Lett.*, vol. 5, pp. 90–92, Mar. 1995.

[3] ——, "Interpreting and improving the PML absorbing boundary condition using anisotropic lossy mapping of space," *IEEE Trans. Magn.*, vol. 32, pp. 968–974, May 1996.

[4] X. Xu, "New approximations in finite element calculation in high frequency," Ph.D. dissertation, South Bank Univ., London, U.K., 1997.

Design and Modeling of Twin-Spiral Coplanar-Waveguide-to-Slotline Transitions

Yo-Shen Lin and Chun Hsiung Chen

***Abstract*—A novel reduced-size twin-spiral coplanar-waveguide-to-slotline transition is proposed in this paper. This twin-spiral transition is based on a modification of quarter-wavelength transformer structure. For design purpose, a hybrid equivalent-circuit model of combining transmission-line theory and full-wave simulation is established. Based on this model, various twin-spiral transition structures are carefully examined theoretically and experimentally. Specifically, a twin-spiral transition with 2.26 : 1 bandwidth and one-quarter the size of conventional ones is achieved. Being simple in fabrication and small in size, the proposed twin-spiral coplanar-waveguide-to-slotline transition is a useful component in uniplanar microwave integrated circuit/monolithic-microwave integrated-circuit applications.**

***Index Terms*—Coplanar waveguide, size reduction, slotline, transition.**

I. Introduction

Uniplanar lines such as coplanar waveguide (CPW), coplanar stripline, and slotline receive increased attention due to their potential applications in many microwave integrated circuits [1]. In 1987, Hirota *et al.* [2] proposed the "uniplanar monolithic-microwave integrated-circuit (MMIC)" configuration, which made use of CPW's and slotlines instead of microstrip lines. These uniplanar structures have some exclusive features over the conventional microstrip-based MMIC. Among the uniplanar lines, the CPW has the advantage of easy integration with solid-state devices, but it suffers from difficulty due to parasitic odd-mode excitation at the discontinuities, such as CPW bending, thus, additional airbridges/bondwires are needed, which complicate the fabrication process. Slotline has the disadvantages of low Q and high radiation loss, and is difficult to mount devices in series configuration; however, it is a good candidate for broad-band antenna applications. To fully utilize the advantages of CPW's and slotlines in a uniplanar microwave integrated circuit (MIC)/MMIC system, implementation of broad-band, low-loss, and compact CPW-to-slotline transition is of practical significance.

Various CPW-to-slotline transitions have been proposed and investigated, and their potential applications in microwave circuits were also reported [3]–[5]. All these transitions to date made use of a $\lambda/4$ transformer structure [6]–[9] or a circular/unterminated slotline open [3], [7], [10], [11]. In [6], the authors experimentally compared various transition structures and found that the transition that made use of a slotline-radial-open with radius of $\lambda/4$ would give a wider bandwidth of 5.5 : 1. The transition that utilized a complex combination of multiple-$\lambda/4$-stub structures in [9] was attractive in improving the transition bandwidth even up to 7.7 : 1 (corresponding to 10-dB return loss). The ideally "all pass" double-Y junction transition [10] used a circular-slotline-open, which not only occupies a large area, but also limits the bandwidth. All these transitions reported occupy a large-circuit area and lead to the inefficient use of high-cost substrate and active layers. Furthermore, the broadband slotline-radial-open transition [6] also suffers from the disadvantage of high radiation loss. This means that the

Manuscript received September 25, 1998; revised December 10, 1999. This work was supported by the National Science Council of Taiwan, R.O.C., under Grant NSC 88-2219-E-002-022.

The authors are with the Department of Electrical Engineering, National Taiwan University, Taipei, Taiwan 10617, R.O.C.

Publisher Item Identifier S 0018-9480(00)02058-5.

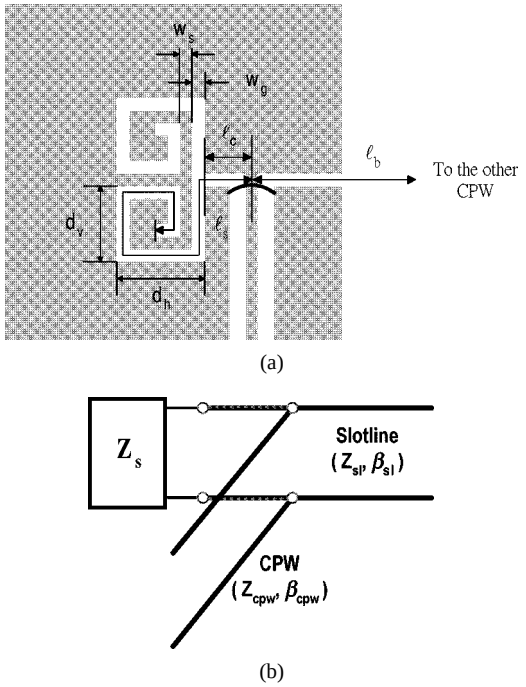

Fig. 1. (a) Geometry of twin-spiral transition structure. (b) Corresponding hybrid equivalent-circuit model.

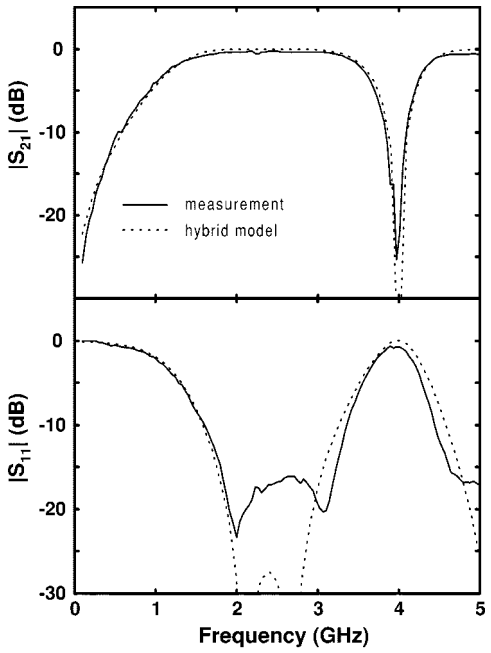

Fig. 2. Measured and simulated results for back-to-back twin-spiral transition structure ($\varepsilon_r = 10.2$, $h = 1.27$ mm, $w_g = w_s = 0.6$ mm, $d_v = 3.6$ mm, $d_h = 4.2$ mm, $\ell_b = 18.35$ mm, $\ell_c = 1.625$ mm, $\ell_s = 18.425$ mm).

spacing between the transition and other components in a circuit must be large enough to avoid the crosstalk problems. Therefore, a compact CPW-to-slotline transition with broad bandwidth and low loss is attractive in the implementation of uniplanar MIC/MMIC's.

In this study, a novel twin-spiral CPW-to-slotline transition with small size and moderate bandwidth is proposed to provide a compact and effective interconnection between the CPW and slotline. This twin-spiral transition is developed based on a modification of the conventional $\lambda/4$ transformer structure. For design purpose, a hybrid equivalent transmission-line circuit model that combines the full-wave technique and transmission-line theory is also established. Several twin-spiral transitions with different physical dimensions are designed and fabricated, and their performances are carefully examined.

II. Twin-Spiral Transition Structures

The twin-spiral CPW-to-slotline transition structure, shown in Fig. 1(a), is the main concern of this study. Basically, reduction of the transition size is achieved by bending the $\lambda/4$ slotline short stub into the form of a spiral structure. To give better transition performance, two spiral lines are connected in series such that the twin-spiral structure acts as an effective open circuit for a wider frequency range. For suppressing the effect of coupled slotline mode excited at the CPW–slotline junction, bondwires at suitable positions are included in the transition structure. The twin-spiral structure is characterized by the parameters: gapwidth w_g, strip width w_s, vertical and horizontal spiral dimensions d_v and d_h, spiral length ℓ_s, and the distance to spiral ℓ_c. For the back-to-back configuration, the slotline length between two CPW's is denoted by ℓ_b.

A simple transmission-line model is inadequate in characterizing the twin-spiral structure due to the complex discontinuities introduced in the transition. Here, we propose a hybrid equivalent transmission-line circuit model [see Fig. 1(b)] in which the twin-spiral part is treated by the full-wave simulation and represented by an impedance function Z_s, while the remaining part is handled by the conventional transmission-line model. This hybrid model is based on the following assumptions. First, the CPW and slotline sections are modeled as transmission lines despite of the non-TEM nature of slotline. Second, the discontinuity effects of the CPW-slotline T-junction and bondwires are neglected. Third, the interactions between the twin-spiral section and the transmission lines are not taken into consideration. The characteristic impedances $Z_{\rm cpw}$, $Z_{\rm sl}$ and phase constants $\beta_{\rm cpw}$, $\beta_{\rm sl}$ of the CPW and slotline are calculated by the close-form formulas [12], [13]. The input impedance Z_s of the twin-spiral section is calculated, using the mixed-potential integral-equation (MPIE) full-wave simulation together with the matrix pencil technique [14]–[16]. In this full-wave simulation, the conductor is assumed to be perfectly conducting and of zero thickness, and the dielectric loss is not included in the calculations.

III. Results

The characteristics of twin-spiral transition structure will be carefully examined both theoretically and experimentally. In the following discussion, the twin-spiral structure is placed on a duroid substrate of thickness $h = 1.27$ mm and dielectric constant $\varepsilon_r = 10.2$. The CPW used in the subsequent study has the following dimensions: strip width $= 0.45$ mm and slot width $= 0.8$ mm, hence, its characteristic impedance is 75 Ω [12]. The slotline has a slot width of 0.5 mm, and its characteristic impedance is 75 Ω at 3 GHz according to the formula in [13]. For measurement, the back-to-back twin-spiral transition structure is constructed in which the slotline length ℓ_b between two CPW's is 18.35 mm. The measurement is done on a HP8510C Network Analyzer, and the thru-reflect-line (TRL) technique is used to calibrate out the effect of coaxial-to-CPW transition.

Shown in Fig. 2 are the measured and simulated results for the back-to-back twin-spiral transition structure designed with $\ell_s = 18.425$ mm, which equals to a quarter of slotline wavelength at 2.18 GHz. The transition exhibits, as expected, a bandpass behavior. The 1-dB passband is in the 1.5–3.4-GHz frequency range, and the corresponding relative bandwidth is 2.26 : 1. The return loss is better than 15 dB in the 1.8–3.2-GHz frequency range. The size of this transition is $(\lambda_s/12.4) \cdot (\lambda_s/6.7) \cong \lambda_s^2/83$, which is about one-quarter of the conventional ones. Good agreement between measured and

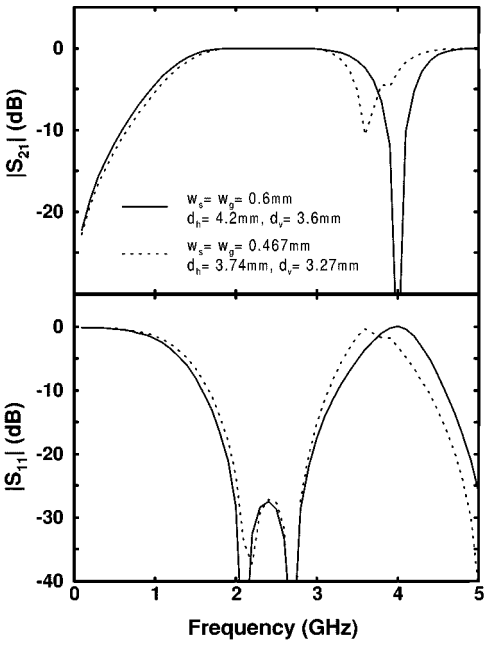

Fig. 3. Simulated results for back-to-back twin-spiral transitions with different spiral size ($\varepsilon_r = 10.2$, $h = 1.27$ mm, $\ell_b = 18.35$ mm, $\ell_c = 1.625$ mm, $\ell_s = 18.425$ mm).

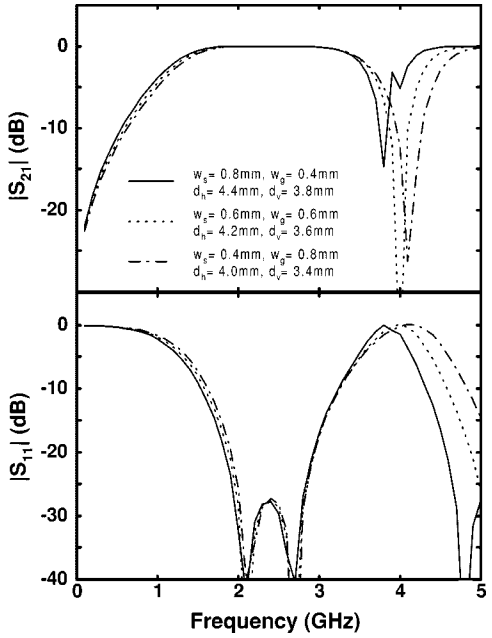

Fig. 4. Simulated results for back-to-back twin-spiral transitions with different gapwidth w_g ($\varepsilon_r = 10.2$, $h = 1.27$ mm, $\ell_b = 18.35$ mm, $\ell_c = 1.625$ mm, $\ell_s = 18.425$ mm).

simulated $|S_{21}|$ up to 5 GHz is observed. There is some discrepancy in $|S_{11}|$, but the simulated result is still satisfactory in predicting the transition behavior in the first passband. In the higher frequency range, the transmission-line assumptions of CPW and slotline may fail, also the radiation and surface-wave losses may become serious, making the hybrid equivalent-circuit model no longer feasible. In this model, only the twin-spiral section is simulated by the full-wave technique, thus, the required central processing unit (CPU) time may be drastically reduced. This hybrid model is an effective tool for analyzing the twin-spiral transition in the first passband, which is the frequency range of interest.

Although Fig. 2 shows a passband centered at about 2.2 GHz, we found from the full-wave simulation that Z_s approaches infinity at about 3 GHz. Physically, the series parasitic capacitance between the strips in the twin-spiral section reduces the effective electrical length of the spiral stubs, leading to an increase in the resonant frequency. In addition, the back-to-back configuration also produces a shift in passband frequency. For a single transition, its passband center frequency will be the resonant frequency of the twin-spiral structure, which can be found by a full-wave simulation of Z_s. Practically, to design a single twin-spiral transition with the resonant frequency at f_0, the spiral length ℓ_s of transition can be estimated by the formula $\ell_s \cong 1.4 \cdot (\lambda_s/4)$, where λ_s is the slotline wavelength corresponding to f_0.

The size of twin-spiral transition can further be reduced if we adopt more turns and smaller strip width w_s and gapwidth w_g in the spiral section. Fig. 3 shows the simulated responses of two back-to-back twin-spiral transition structures with the same spiral length $\ell_s = 18.425$ mm, but different spiral parameters. The size of transition with $w_s = w_g = 0.467$ mm is $(\lambda_s/16)\cdot(\lambda_s/8.6)$, which is about 1/1.66 that of the one with $w_s = w_g = 0.6$ mm and a size of $(\lambda_s/12.4)\cdot(\lambda_s/6.7)$. Note that both transitions have nearly the same center frequency at 3 GHz, but the one with a smaller spiral size exhibits a smaller bandwidth. This results from an increase of parasitics when the size of the twin-spiral structure is reduced. Thus, in designing a twin-spiral transition, we have to compromise between size and bandwidth.

Fig. 4 shows the effect of gapwidth w_g on the performance of twin-spiral transition. Three back-to-back transitions with the same spiral length ℓ_s and equal turn number in the spiral section are simulated by the hybrid model. The gapwidth w_g is varied from 0.4 to 0.8 mm, and other parameters such as w_s, d_v, and d_h are changed accordingly to keep the shape of twin-spiral structure unchanged. The simulated responses of these three transitions are shown in Fig. 4 for comparison. The one with a larger w_g exhibits a broader bandwidth. This is a consequence of increasing the input impedance Z_s of the twin-spiral section for larger w_g.

The design of twin-spiral transitions presents a tradeoff between size and bandwidth. With a fixed transition size, the bandwidth can be optimized by choosing a larger w_g. The performance of transition can easily be characterized by the proposed hybrid model.

IV. Conclusion

In this study, novel twin-spiral CPW-to-slotline transition structures have been proposed and carefully examined. For design and modeling purposes, a hybrid equivalent transmission-line circuit model has also been established. The implementation into twin-spiral transition is an easy and effective way to reduce the size of CPW-to-slotline transition with size reduction factor in the order of 1/3 to 1/4. There is some compromise between size and bandwidth, and the transition size can further be reduced if the requirement on bandwidth may be looser. The reduced-size twin-spiral transition structure is attractive in MIC/MMIC applications.

Acknowledgment

The full-wave simulation in this study was carried out by the software developed by Dr. F.-L. Lin. Discussions with Dr. Lin were helpful and are very much appreciated by the authors.

References

[1] K. C. Gupta, R. Garg, and I. J. Bahl, *Microstrip Lines and Slotlines*, 2nd ed. Norwood, MA: Artech House, 1996, ch. 5 and 7.

[2] T. Hirota, Y. Tarusawa, and H. Ogawa, "Uniplanar MMIC hybrids—A proposed new MMIC structure," *IEEE Trans. Microwave Theory Tech.*, vol. MTT-35, pp. 576–581, June 1987.

[3] H. Ogawa and A. Minagawa, "Uniplanar MIC balanced multiplier—A proposed new structure for MIC's," *IEEE Trans. Microwave Theory Tech.*, vol. MTT-35, pp. 1363–1368, Dec. 1987.
[4] C.-H. Ho, L. Fan, and K. Chang, "Broad-band uniplanar hybrid-ring and branch-line couplers," *IEEE Trans. Microwave Theory Tech.*, vol. 41, pp. 2116–2125, Dec. 1993.
[5] L. Fan, C.-H. Ho, S. Kanamaluru, and K. Chang, "Wide-band reduced-size uniplanar magic-T, hybrid-ring, and de Ronde's CPW-slot couplers," *IEEE Trans. Microwave Theory Tech.*, vol. 43, pp. 2749–2758, Dec. 1995.
[6] C.-H. Ho, L. Fan, and K. Chang, "Experimental investigations of CPW-slotline transitions for uniplanar microwave integrated circuits," *IEEE MTT-S Int. Microwave Symp. Dig.*, pp. 877–880, 1993.
[7] W. Grammer and K. S. Yngvesson, "Coplanar waveguide transitions to slotline: Design and microprobe characterization," *IEEE Trans. Microwave Theory Tech.*, vol. 41, pp. 1653–1658, Sept. 1993.
[8] V. Trifunovic and B. Joknaovic, "Review of printed Marchand and double Y baluns: Characteristics and application," *IEEE Trans. Microwave Theory Tech.*, vol. 42, pp. 1454–1462, Aug. 1994.
[9] K. Hettak, J. P. Coupez, T. L. Gouguec, S. Toutain, P. Legaud, and E. Penard, "Improved CPW to slotline transitions," *IEEE MTT-S Int. Microwave Symp. Dig.*, pp. 1831–1834, 1996.
[10] V. Trifunovic and B. Joknaovic, "New uniplanar balun," *Electron. Lett.*, vol. 28, no. 10, pp. 813–815, May 1991.
[11] T. Q. Ho and S. M. Hart, "A broad-band coplanar waveguide to slotline transition," *IEEE Microwave Guided Wave Lett.*, vol. 2, pp. 415–416, Oct. 1992.
[12] C. Veyres and V. F. Hanna, "Extension of the application of conformal mapping techniques to coplanar lines with finite dimensions," *Int. J. Electron.*, vol. 48, no. 1, pp. 47–56, July 1980.
[13] R. Janaswamy and D. H. Schaubert, "Characteristic impedance of a wide slotline on low-permittivity substrate," *IEEE Trans. Microwave Theory Tech.*, vol. MTT-34, pp. 900–902, Aug. 1986.
[14] T. Itoh, "Spectral domain immittance approach for dispersion characteristics of generalized printed transmission lines," *IEEE Trans. Microwave Theory Tech.*, vol. MTT-28, pp. 733–736, July 1980.
[15] K. Sarkar, Z. A. Maricevic, and M. Kahrizi, "An accurate de-embedding procedure for characterizing discontinuities," *Int. J. Microwave Millimeter-Wave Computer-Aided Eng.*, vol. 2, no. 3, pp. 135–143, Mar. 1992.
[16] F. L. Lin, C. W. Chiu, and R. B. Wu, "Coplanar waveguide bandpass filter—A ribbon of brick wall design," *IEEE Trans. Microwave Theory Tech.*, vol. 43, pp. 1589–1596, July 1995.

An Efficient Characterization of Interconnected Multiconductor-Transmission-Line Networks

A. Orlandi and C. R. Paul

***Abstract*—The numerical solution of the multiconductor-transmission-line (MTL) equations for lossy interconnected transmission lines (TL's) is investigated in this paper. The solution for the transmission-line segments is accomplished through the finite-difference time-domain method, whereas the terminations and interconnection networks (which may contain nonlinearities) are characterized with an efficient state-variable representation. High-frequency skin-effect losses in the TL's are included in the MTL equations through convolution integrals in the MTL equations. The computation of these convolution integrals represents the bulk of the solution effort. Two methods, the singular-value-decomposition method and the matrix-pencil method, are shown to significantly reduce the computation time and improve the solution accuracy.**

I. Introduction

Due to increasing clock and data speeds, the spectral content of today's high-speed digital systems extends well into the gigahertz frequency range. Increasing density of integrated circuits results in smaller interconnect cross-sectional dimensions, which increase losses. In particular, the skin-effect loss, due to the increase in the high-frequency interconnect resistance as the square root of frequency, becomes increasingly more important. This square-root-of-frequency dependence of the line per-unit-length resistance and internal inductance presents considerable computational problems in the time domain; its inclusion into the frequency-domain characterization of the multiconductor transmission lines (MTL's) is trivial. In this paper, we present a computationally efficient method for the solution of MTL's that are interconnected with arbitrary networks. The numerical solution of the MTL equations is accomplished through the finite-difference time-domain (FDTD) method, whereas the terminations and interconnection networks (which may contain nonlinearities) are characterized with an efficient state-variable representation. In recent publications [1], [2], an FDTD analysis of lossy MTL networks in the presence of general loads and interconnection networks has been presented. In both papers, the lines' loads and interconnections have been described by a state-variable formulation.

In this paper, the recursive convolution integral procedure implemented in [1] and [2] to handle the frequency-dependent losses of the line is improved upon. The majority of the computing time for solution of the overall network is consumed by the evaluation of the convolution integral. In this paper, an alternative technique is presented to speed up such a calculation. Two methods, the singular-value-decomposition (SVD) method and the matrix pencil (MP) method, are shown to significantly reduce the computation time and improve the solution accuracy.

In Section II, we summarize the FDTD model of the MTL's of the network. The state-variable equations of loads and interconnections are discretized by means of the second-order Adams–Moulton method [3]. Section III contains the evaluation of a smaller and more accurate set of coefficients to exponentially approximate the kernel of the convolution using two methods: the SVD and MP methods. Section IV shows the improvement for a transmission-line network.

Manuscript received September 29, 1998; revised December 10, 1999.

A. Orlandi is with the Department of Electrical Engineering, University of L'Aquila I-67040, Poggio di Roio, L'Aquila, Italy.

C. R. Paul is with the Department of Electrical and Computer Engineering, Mercer University, Macon, GA 31207 USA.

Publisher Item Identifier S 0018-9480(00)02060-3.

TABLE I
COEFFICIENTS FOR THE EXPONENTIAL APPROXIMATION (9)

	Prony [5, pg. 174]		Prony-SVD N=8		Matrix Pencil N=8		Matrix Pencil N=5	
N	a_i	α_i	a_i	α_i	a_i	α_i	a_i	α_i
1	0.07909818000000	-0.00114844270000	0.09443731352010	-0.00158216329679	0.83141575527524	-3.87729651101032	1.10557125424941	-2.48092662001828
2	0.11543423000000	-0.01381832900000	0.15665433541329	-0.02182158099232	0.36307454340158	-1.02223794772756	0.46769297045694	-0.35506470843002
3	0.13435380000000	-0.05403759600000	0.16504026887586	-0.09215781035531	0.27397819247920	-0.38821711577327	0.22921612744350	-0.07148401617605
4	0.21870422000000	-0.14216494000000	0.28881469355189	-0.25144385667250	0.18917985781622	-0.15317357362479	0.11784227513357	-0.01395977802476
5	0.09822966700000	-0.30128437000000	0.07425894610077	-0.54918916889548	0.12665223879163	-0.06053520868332	0.07961871318460	-0.00117259103590
6	0.51360484000000	-0.56142185000000	0.47247797195978	-1.07005583786812	0.06001291022045	-0.00069394020132		
7	-0.20962898000000	-0.97117126000000	-0.01995013624566	-2.03571363549832	0.06781098098833	-0.00678636372664		
8	1.19744470000000	-1.63384330000000	0.76826675584837	-5.42397696795711	0.08787552084192	-0.02271126509422		
9	0.01122549100000	-2.89513290000000						
10	-0.74425255000000	-5.04109690000000						
$Z_0(0)$	1.4114280601		2.00000014902439		1.99999999981455		1.99994134046802	

II. COMPUTATIONAL MODEL

An MTL network can be considered that is made up of parts in which the propagation of voltage and current cannot be neglected and parts in which this can be disregarded. The former are the transmission lines (TL's) or *tubes*, and the latter are represented by lumped circuits, which are called *junctions*. A junction connects two or more tubes. A *termination* is a particular junction with only one tube connected.

Consider a tube formed by an $(n+1)$ conductor uniform TL whose equations for the general case of imperfect conductors immersed in an incident field are [4]

$$\frac{\partial}{\partial z}\mathbf{V}(z,t) + \mathbf{Z}_i(t) * \mathbf{I}(z,t) + \mathbf{L}\frac{\partial}{\partial t}\mathbf{I}(z,t) = -\frac{\partial}{\partial z}\mathbf{E}_T(z,t) + \mathbf{E}_L(z,t) \tag{1a}$$

$$\frac{\partial}{\partial z}\mathbf{I}(z,t) + \mathbf{C}\frac{\partial}{\partial t}\mathbf{V}(z,t) = -\mathbf{C}\frac{\partial}{\partial t}\mathbf{E}_T(z,t) \tag{1b}$$

where $\mathbf{V}$ and $\mathbf{I}$ are $n \times 1$ vectors of the line voltages (with respect to the reference conductor) and line currents, respectively. The position along the line is denoted as z. The per-unit-length parameter matrices are $\mathbf{L}$ (inductance) and $\mathbf{C}$ (capacitance). The conductor losses are represented by $\mathbf{Z}_i(t)$, which is the inverse Laplace transform of $\mathbf{Z}_i(s) = \mathbf{R}(s) \div s\mathbf{L}_i(s)$, where s is the Laplace transform variable. This conductor internal impedance contains both resistance $\mathbf{R}$ and internal inductance $\mathbf{L}_i$. Incident field excitation is included via the quantities $\mathbf{E}_T(z,t)$ and $\mathbf{E}_L(z,t)$, which are $n \times 1$ vectors containing the components of the incident electric field that are transverse to the line and parallel to the line conductors, respectively, with the line conductors removed [1], [4].

The finite-difference equation (FDE) of (1), obtained by using a central difference scheme, becomes, for the interior points in which the line's conductors are divided [1]

$$\begin{aligned}\left(\frac{\Delta z}{\Delta t}\mathbf{L} + \frac{\Delta z}{2}\mathbf{A} + \frac{\Delta z}{\sqrt{\pi\Delta t}}Z_0(0)\mathbf{B}\right)\mathbf{I}_k^{n+3/2} &= \left(\frac{\Delta z}{\Delta t}\mathbf{L} - \frac{\Delta z}{2}\mathbf{A} + \frac{\Delta z}{\sqrt{\pi\Delta t}}Z_0(0)\mathbf{B}\right)\mathbf{I}_k^{n+1/2} \\ &- \frac{\Delta z}{\sqrt{\pi}\sqrt{\Delta t}}\mathbf{B}\sum_{m=1}^{n} Z_0(m)\left[\mathbf{I}_k^{n+3/2-m} - \mathbf{I}_k^{n+1/2-m}\right] \\ &- \left(\mathbf{V}_{k+1}^{n+1} - \mathbf{V}_k^{n+1}\right) - \left[\mathbf{E}_{T,k+1}^{n+1} - \mathbf{E}_{T,k}^{n+1}\right] \\ &+ \frac{\Delta z}{2}\left[\mathbf{E}_{L,k}^{n+3/2} + \mathbf{E}_{L,k}^{n+1/2}\right]\end{aligned} \tag{2a}$$

$$\mathbf{V}_k^{n+1} = \mathbf{V}_k^n - \frac{\Delta t}{\Delta z}\mathbf{C}^{-1}\left(\mathbf{I}_k^{n+1/2} - \mathbf{I}_{k-1}^{n+1/2}\right) - \left[\mathbf{E}_{T,k}^{n+1} - \mathbf{E}_{T,k}^n\right] \tag{2b}$$

where we denote $\mathbf{V}_k^n \equiv \mathbf{V}((k-1)\Delta z, n\Delta t)$, $\mathbf{I}_k^n \equiv \mathbf{I}((k-1/2)\Delta z, n\Delta t)$. The transverse incident field sources $\mathbf{E}_T(z,t)$ are to be evaluated at the voltage positions, whereas the longitudinal field sources $\mathbf{E}_L(z,t)$ are to be evaluated at the current positions, i.e., $\mathbf{E}_{T,k}^n \equiv \mathbf{E}_T((k-1)\Delta z, n\Delta t)$, $\mathbf{E}_{L,k}^n \equiv \mathbf{E}_L((k-1/2)\Delta z, n\Delta t)$. In (2), $Z_0(m)$ are terms stemming from the Prony's approximation of the convolution in (1) [5]. We will show an improved method of evaluating these contributions. The incorporation of the terminal conditions has been extensively discussed in [1], [4], and [6].

The characterization of the lumped circuits inside the junctions is accomplished by the state-variable formulation [1]–[3]

$$\dot{\mathbf{X}}(t) = \mathbf{M}\mathbf{X}(t) + \mathbf{N}\mathbf{U}(t) \tag{3a}$$

$$\mathbf{I}(t) = \mathbf{O}\mathbf{X}(t) + \mathbf{P}\mathbf{U}(t) + \mathbf{Q}\dot{\mathbf{U}}(t) \tag{3b}$$

where "dots" indicate time derivatives. The vector $\mathbf{X}$ contains the state variables of the junction, the vector $\mathbf{U}$ contains the input sources of the network, and the vector $\mathbf{I}$ contains the designated outputs: the currents at the connection nodes between junctions and tubes. The central difference scheme used for the FDE (2) is accurate to order $O(h^2)$; to maintain the same order of accuracy within all the procedure, the second-order Adams–Moulton scheme is used to obtain the FDE associated with (3). This is a single-point, single-step, implicit, and unconditionally stable scheme. By applying this method to (3), they become, for the mth junction,

$$\mathbf{X}_m^{n+1} = \mathbf{X}_m^n + \frac{\Delta t}{2}\mathbf{M}_m\left[\mathbf{X}_m^{n+1} + \mathbf{X}_m^n\right] + \frac{\Delta t}{2}\mathbf{N}_m\left[\mathbf{U}_m^{n+1} + \mathbf{U}_m^n\right] \tag{4a}$$

$$\frac{1}{2}\left[\mathbf{I}_m^{n+1} + \mathbf{I}_m^n\right] = \frac{1}{2}\mathbf{O}_m\left[\mathbf{X}_m^{n+1} + \mathbf{X}_m^n\right] + \frac{1}{2}\mathbf{P}_m\left[\mathbf{U}_m^{n+1} + \mathbf{U}_m^n\right] + \frac{1}{\Delta t}\mathbf{Q}_m\left[\mathbf{U}_m^{n+1} - \mathbf{U}_m^n\right] \tag{4b}$$

where vector $\mathbf{U}_m = [\mathbf{S}_m\mathbf{V}_m]^t$ contains the inputs for the state-variable representation: the independent sources inside the junction $\mathbf{S}_m$ and the tube voltages $\mathbf{V}_m = [\mathbf{V}_{m,i}\mathbf{V}_{m,j}\mathbf{V}_{m,k}\mathbf{V}_{m,l}]^t$ at the connection nodes between attached I, j, k, and l tubes and the junction. The vectors $\mathbf{I}_m$ contain the line currents of the tubes connected to the junction m evaluated at the connection nodes.

III. Exponential Approximation for the Conductor Losses Convolution Term $\mathbf{Z}_i(t) * \mathbf{I}(z,t)$

In the evaluation of the FDE associated with (1), a significant portion of the computing time is spent in evaluating the convolution of the transient impedance $\mathbf{Z}_i(t)$ and the current $\mathbf{I}(z,t)$ in (1a). A common way of representing the skin-effect losses of the conductors is [7]

$$\mathbf{Z}_i(s) = \mathbf{A} + \mathbf{B}\sqrt{s} \tag{5}$$

and, hence,

$$\begin{aligned} \mathbf{Z}_i(s)\mathbf{I}(z,s) &= \mathbf{A}\mathbf{I}(z,s) + \mathbf{B}\left[\frac{1}{\sqrt{s}}\right] s\mathbf{I}(z,s) \\ &\Updownarrow \\ \mathbf{Z}_i(t) * \mathbf{I}(z,t) &= \mathbf{A}\mathbf{I}(z,t) \\ &\quad + \frac{1}{\sqrt{\pi}}\mathbf{B}\left[\int_0^t \frac{1}{\sqrt{\tau}} \frac{\partial}{\partial(t-\tau)}\mathbf{I}(z,t-\tau)\,d\tau\right]. \end{aligned} \tag{6}$$

The convolution in (1a) is approximated in the following manner where the function $\mathbf{F}(t)$ (which represents the derivative of the line current in the MTL equations) is approximated as constant over the Δt segments [4]:

$$\begin{aligned} \int_0^t \frac{1}{\sqrt{\tau}}\mathbf{F}(t-\tau)\,d\tau &\cong \int_0^{(n+1)\Delta t} \frac{1}{\sqrt{\tau}}\mathbf{F}\Big((n+1)\Delta t - \tau\Big)\,d\tau \\ &\cong \sum_{m=0}^{n} \mathbf{F}^{n+1-m} \int_{m\Delta t}^{(m+1)\Delta t} \frac{1}{\sqrt{\tau}}\,d\tau \\ &= \sqrt{\Delta t}\sum_{m=0}^{n} \mathbf{F}^{n+1-m} Z_0(m) \end{aligned} \tag{7}$$

where

$$Z_0(m) = \int_m^{(m+1)} \frac{1}{\sqrt{\varsigma}}\,d\varsigma = 2\left(\sqrt{m+1} - \sqrt{m}\right) \tag{8}$$

If $Z_0(m)$ is approximated by a series of exponentials

$$Z_0(m) = \sum_{i=1}^{N} a_i e^{\alpha_i m} \tag{9}$$

the convolution in (6) is evaluated using a recursive algorithm [8]. In order to determine the coefficients a_i and the time constants α_i in (9), different techniques can be used. In [5], Prony's method is applied to (8) for $M = 500$ samples and $N = 10$ terms. The resulting coefficients are reported in Table I. Fig. 1 shows the relative error between the exact value of $Z_0(m)$ in (8) and the approximation (9) by using the coefficients in [5]. Significant error is associated with the first 50–60 samples; in particular, the exact value of $Z_0(0)$ from (8) is equal to two. However, by using the coefficients proposed in [5, pg. 174], one obtains from (9)

$$Z_0(0) = \sum_{i=1}^{10} a_i = 1.4114280601.$$

An error in $Z_0(0)$ and in the subsequent values of $Z_0(m)$ has two main repercussions: it affects all the values of the lines' currents because of the term $(\Delta z/\Delta t)Z_0(0)\mathbf{B}$ in (2a) [9] and the early-time response of the convolution $\mathbf{Z}_i(t) * \mathbf{I}(z,t)$ when the frequency-dependent losses of the conductors have the most important role. Although not shown in the figure, the relative error for the values of $Z_0(m)$ extrapolated for $m > M$ is even worse. The solution of a least-square problem directly from the *normal equations* in the Prony method is rather susceptible to roundoff error and to the condition number of the coefficients matrix [10]. An alternative technique is the SVD [11]. SVD produces a solution of an overdetermined problem that is the best approximation in the least-square sense; it also fixes the roundoff problems for the first samples (as demonstrated by the values of $Z_0(m)$ in Table I) and is suitable for dealing with nearly singular matrices. Following these considerations, a Prony's method with SVD (Prony–SVD) has been implemented and an eight-exponential-term approximation of (8) was computed. Fig, 1 also shows the relative error between the exact values given by (8) and the Prony–SVD approximation.

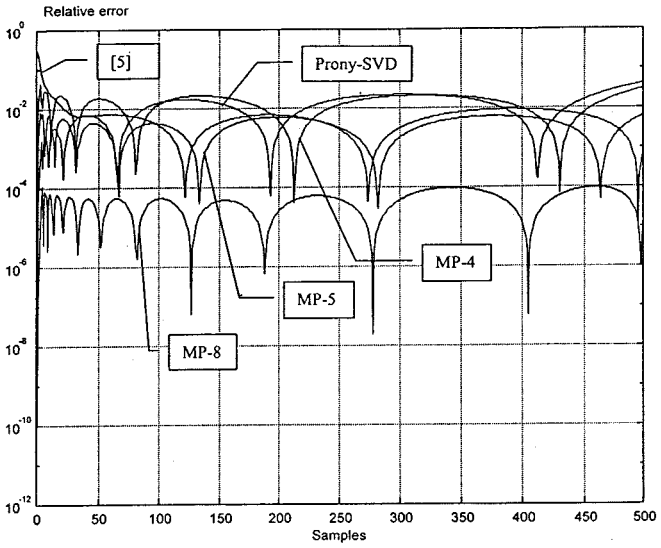

Fig. 1. Relative error between the exact value of $Z_0(m)$ from (8) and that evaluated in [54] ($N = 10$), evaluated by Prony–SVD ($N = 8$), by MP-8 ($N = 8$), by MP-5 ($N = 5$), and by MP-4 ($N = 4$).

To improve the estimation of a_i and α_i, in order to have a better approximation of $Z_0(m)$ with a least number N of terms in (9), the MP method [12] is used. In this method, the α_i coefficients are found in one step as the solution of a generalized eigenvalue problem. This process is more computationally efficient and accurate compared to the Prony method, which is a two-step procedure in finding the poles $e^{\alpha_i m}$. Fig. 1 also compares the previously computed relative errors between the exact function $Z_0(m)$ and the approximation given by [5] and by Prony–SVD with the same relative errors associated with (9) by using the coefficients evaluated by MP with $N = 8$ (MP-8), $N = 5$ (MP-5), and $N = 4$ (MP-4). As expected, the approximation MP-8 is much better than [5] (which has $N = 10$) and the Prony–SVD that uses $N = 8$ terms. MP-5 shows a better fitting of $Z_0(m)$ than [5] in the initial values and the same order of error for the late time. It is interesting to point out that MP-4 also gives a better early-time approximation of $Z_0(m)$ than [5]; unfortunately, the late-time error is not acceptable. Table I summarizes the coefficients proposed by [5] and evaluated by Prony–SVD and MP for $N = 8$ and $N = 5$. In the last row of the table, the values of $Z_0(0)$ computed by means of (10) are given.

In the following calculations of the transient response of an MTL network, the MP method is used to evaluate the coefficients a_i and α_i with $N = 5$ terms in the exponential approximation. This significantly reduces the computation time as reported in Table II.

IV. Computed Results

The above formulation is applied to the prediction of crosstalk and the transient response of an MTL network. Although the excitations in the above formulation can be either independent sources internal to the junctions/terminations or external incident electromagnetic fields, the following example uses lumped sources. The FDTD model is validated for incident field excitation, as well as other configurations in [1], [2], and [4].

A network configuration that is typical of clock distribution structures on printed circuit boards is shown in Fig. 2. All of the tubes are

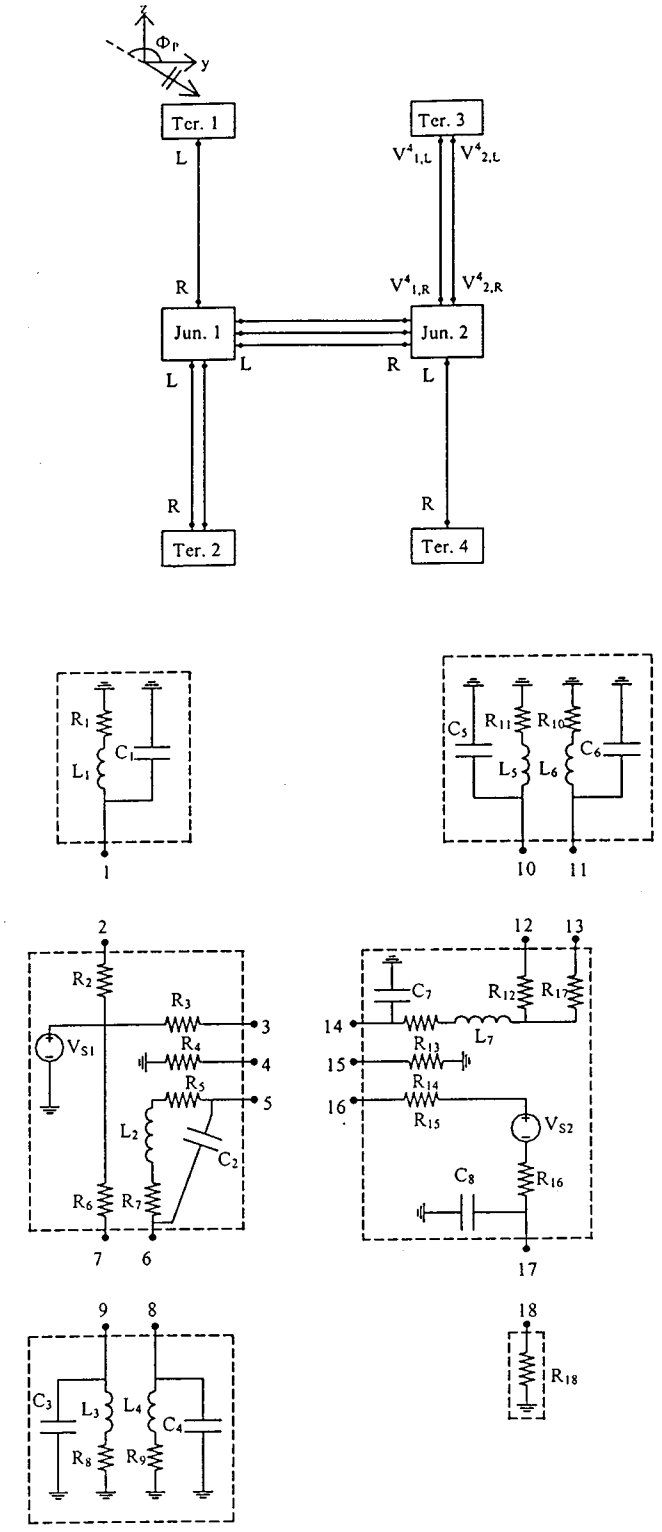

Fig. 2. MTL network considered (node numbering and junctions/terminations lumped circuits).

0.245-cm long and the per unit length parameter matrices C and L are tubes $T1$ and $T5$ $(n = 1)$

$$\mathbf{L}_1 = \mathbf{L}_5 = 0.930767\ \mu\text{H/m}$$
$$\mathbf{C}_1 = \mathbf{C}_5 = 11.9541\ \text{pF/m}$$

TABLE II
NUMBER OF COEFFICIENTS VERSUS RELATIVE COMPUTING TIME

Number of coefficients N	Relative CPU time
10	1
8	0.812
5	0.533

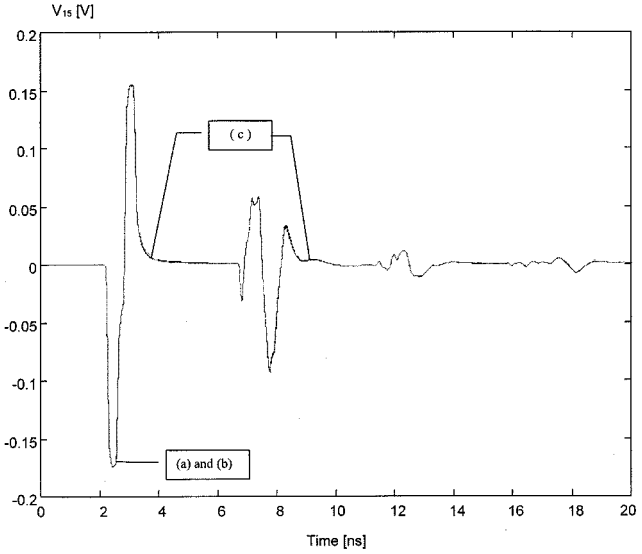

(a)

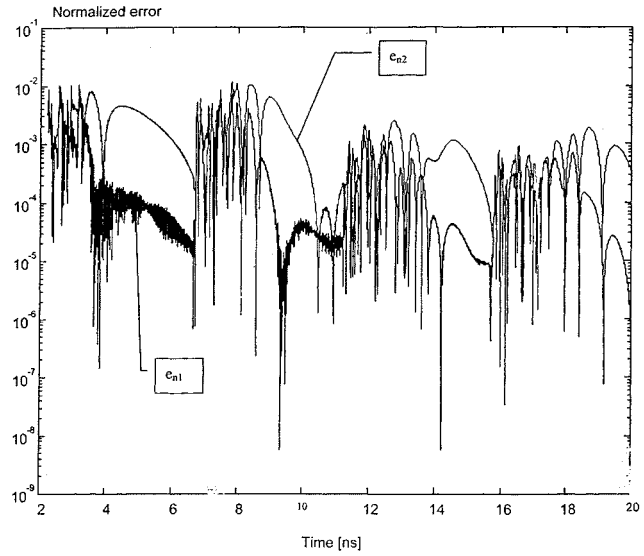

(b)

Fig. 3. (a) Transient voltage V_{15} evaluated by means of the coefficients: a in [5], b from MP-5, and c from Prony-SVD (see Table I). (b) Normalized errors e_{n1} and e_{n2}.

tube $T2$ $(n = 3)$

$$\mathbf{L}_2 = \begin{bmatrix} 0.930767 & 0.160944 & 0.069314 \\ 0.160944 & 0.930767 & 0.160944 \\ 0.069314 & 0.160944 & 0.930767 \end{bmatrix} \mu\text{H/m}$$

$$\mathbf{C}_2 = \begin{bmatrix} 12.3486 & -2.03716 & -0.056735 \\ -2.03716 & 12.6586 & -2.03716 \\ -0.056735 & -2.03716 & 12.3486 \end{bmatrix} \text{pF/m}$$

tubes $T3$ and $T4$ $(n = 2)$

$$\mathbf{L}_3 = \mathbf{L}_4 = \begin{bmatrix} 0.930767 & 0.160944 \\ 0.160944 & 0.930767 \end{bmatrix} \ \mu\text{H/m}$$

$$\mathbf{C}_3 = \mathbf{C}_4 = \begin{bmatrix} 12.3226 & -2.13076 \\ -2.13076 & 12.3226 \end{bmatrix} \ \text{pF/m}.$$

The resistances inside the junctions/terminations are one of the three following values:

$$R_i = \begin{cases} 50\ \Omega, & i = 1,3,4,8,9,10,11,12,14,17 \\ 25\ \Omega, & i = 2,5,6,7,13,15,16 \\ 279\ \Omega, & i = 18 \end{cases}$$

and the capacitances and inductances have one of the two following values:

$$C_i = \begin{cases} 5.5\ \text{pF}, & i = 1,\cdots,6 \\ 10\ \text{pF}, & i = 7,8 \end{cases}$$

$$L_i = \begin{cases} 80\ \text{nH}, & i = 1,3,\cdots,6 \\ 15\ \text{nH}, & i = 2,7. \end{cases} \tag{10}$$

V_{s1} in junction 2 is a trapezoidal pulse having a rise/fall time $\tau_r = \tau_f = 100$ ps and pulsewidth of $\tau = 500$ ps. Fig. 3(a) compares the transient voltage at node 15 evaluated by using the exponential approximation in (9) with the coefficients in [5] and those evaluated by MP-5 and Prony–SVD (see Table I). The first two are perfectly overlapped and a slight difference among these two waveforms and the third one is observable on the "tails" of each reflection wavelets ($4\ \text{ns} \le t \le 7\ \text{ns}$, $8.5\ \text{ns} \le t \le 10\ \text{ns}$). This difference is better pointed out in Fig. 3(b), where the normalized errors e_{n1} and e_{n2} among the transient data of V_{15} computed via [5] and those computed via MP-5 or Prony–SVD are shown as follows:

$$e_{n1} = \frac{\left| V_{15}^{[5]} - V_{15}^{\text{MP-5}} \right|}{V_{15,\max}^{[5]}}$$

$$e_{n2} = \frac{\left| V_{15}^{[5]} - V_{15}^{\text{Prony-SVD}} \right|}{V_{15,\max}^{[5]}}$$

V. Conclusion

A computationally efficient method for the solution of interconnected MTL networks has been presented in this paper. The numerical solution of the MTL equations is accomplished through the FDTD method, whereas the terminations and interconnection networks (which may contain nonlinearities) are characterized with an efficient state-variable representation. The computation of the convolution integral, which is due to skin-effect losses of the line conductors, was made more efficient and accurate through the use of the SVD and MP methods. The accuracy of each method was demonstrated via a complicated MTL network. These new methods of evaluating the convolution integral also provided a significant reduction in the computation time.

Acknowledgment

The authors acknowledge the numerous helpful discussions of Ing. M. Baccalá.

References

[1] A. Orlandi and C. R. Paul, "FDTD analysis of lossy multiconductor transmission lines terminated in arbitrary loads," *IEEE Trans. Electromag. Compat.*, vol. 38, pp. 388–399, Aug. 1996.

[2] M. Baccalá, A. Orlandi, and C. R. Paul, "Analysis of multiconductor transmission lines networks: State-variable characterization of junctions and terminations," in *Proc. ROMA Int. Symp. EMC*, Rome, Italy, Sept. 14–18, 1998, pp. 615–620.

[3] L. O. Chua and P. M. Lin, *Computed Aided Analysis of Electronic Circuits: Algorithms and computational Techniques*, NJ: Englewood Cliffs, 1975.

[4] C. R. Paul, *Analysis of Multiconductor Transmission Lines*. New York: Wiley, 1994.

[5] K. S. Kunz and R. J. Luebbers, *The Finite Difference Time Domain Method in Electromagnetics*. Boca Raton, FL: CRC Press, 1993.

[6] C. R. Paul, "Incorporation of terminal constraints in the FDTD analysis of transmission lines," *IEEE Trans. Electromag. Compat.*, vol. 36, pp. 85–91, May 1994.

[7] N. S. Nahman and D. R. Holt, "Transient analysis of coaxial cables using the skin effect approximation $A + B\sqrt{s}$," *IEEE Trans. Circuit Theory*, vol. CT-19, pp. 443–451, Sept. 1972.

[8] A. Semlyen and A. Dabuleanu, "Fast and accurate switching transient calculations on transmission lines with ground return using recursive convolution," *IEEE Trans. Power App. Syst.*, vol. PAS-94, pp. 561–571, Feb. 1975.

[9] S. Celozzi and A. Orlandi, "Advances in numerical solution algorithms for time domain MTL equations," *Appl. Comput. Electromag. Soc. Newslett.*, vol. 13, no. 3, Nov. 1998.

[10] F. B. Hildebrand, *Introduction to Numerical Analysis*, 2nd ed. New York: Dover, 1987.

[11] C. L. Lawson and R. Hanson, *Solving Least Squares Problems*, NJ: Englewood Cliffs, 1983.

[12] T. K. Sarkar and O. Pereira, "Using the matrix pencil method to estimate the parameters of a sum of complex exponentials," *IEEE Antennas Propagat. Mag.*, vol. 37, no. 1, pp. 48–55, Feb. 1995.

A Simplified Procedure to Calculate the Power Gain Definitions of FET's

Claudio Paoloni

***Abstract*—A graphical method to easily derive the power gain definitions of field-effect transistors (FET's) is proposed in this paper. This method is applicable to MESFET's and high electron-mobility transistors described by the typical π-model. A new set of simple expressions of the S-parameters, functions of the circuit elements of the FET complete model, is derived. These expressions are presented in graphic form to quickly compute the modules of the FET S-parameters and then the power gains. The accuracy of this approach has been proven by comparison with simulations of the FET complete model.**

***Index Terms*—Microwave FET amplifiers, microwave FET's, scattering parameters.**

I. Introduction

To evaluate field-effect transistor (FET) performance, different definitions of power gain can be used. The well-known expressions are reported here for reference [1].

Transducer power gain in 50-Ω system

$$G_T = |S_{21}|^2. \tag{1}$$

Manuscript received October 13, 1998; revised December 10, 1999.

The author is with the Department of Electronic Engineering, University of Roma "Tor Vergata," 00133 Roma, Italy.

Publisher Item Identifier S 0018-9480(00)02061-5.

Maximum stable gain $(k < 1)$

$$G_{\rm ms} = \frac{|S_{21}|}{|S_{12}|}. \tag{2}$$

Maximum available gain $(k > 1)$

$$G_{\rm ma} = \frac{|S_{21}|}{|S_{12}|}(k - \sqrt{k^2 - 1}) \tag{3}$$

where k is the stability factor

$$k = \frac{1-|S_{11}|^2-|S_{22}|^2+|D|^2}{2|S_{12}||S_{21}|}, \qquad \text{where } D = S_{11}S_{22} - S_{12}S_{21}.$$

Maximum unilateral transducer power gain

$$G_{\rm TU\,max} = \frac{|S_{21}|^2}{(1-|S_{11}|^2)(1-|S_{22}|^2)}. \tag{4}$$

Power gain with input conjugate matched

$$G = \frac{|S_{21}|^2}{1-|S_{11}|^2}. \tag{5}$$

Available power gain with output conjugate matched

$$G_A = \frac{|S_{21}|^2}{1-|S_{22}|^2}. \tag{6}$$

To calculate the power gain according to (1)–(6), the modules of the FET S-parameters are required. The FET complete model [see Fig. 1(a)] is often available to designers and, therefore, the S-parameters must be derived from this model. Of course, due to the complexity of the equations, this must be performed by using a simulation program. It could be useful, especially in a preliminary design phase, when the active devices for the amplifier design must be chosen, to have a method that allows evaluation, in an easy manner and using nothing other than a pocket calculator, of the power gain performance. To make this possible, three circuits simpler than the FET complete model have been introduced. The purpose of each of these circuits is to obtain the same electrical behavior of one or two of the FET S-parameters. The circuit elements of each simple circuit are a function of the FET complete model elements. This allows the generation of expressions describing the S-parameters simpler than the corresponding expressions for the FET complete model. These expressions are also suitable for presentation in graphic form, allowing an immediate calculation of the power gain definitions by (1)–(6).

II. Theory and Results

The S-parameter modules $|S_{11}|$, $|S_{22}|$, $|S_{21}|$, and $|S_{12}|$ must be calculated to obtain the FET power gains by (1)–(6). To generate expressions of the S-parameters simpler than the expressions for the FET complete model, some approximations must be performed. The method consists of finding a simple circuit whose frequency behavior is similar to the frequency behavior of the desired FET S-parameters. The circuit elements of the simple circuit are defined, after some algebraic manipulations, as functions of the elements of the FET complete model.

The design-oriented FET model previously proposed in [2] is suitable to obtain accurate and simple expressions of S_{21} and S_{11}. The expressions to derive the design-oriented FET model from the FET complete model are listed in Fig. 1(b). The expression of S_{21} for the design-oriented FET model is shown in (7), at the bottom of the following page, where g_m is the FET transconductance, $C_{\rm gse}$, $C_{\rm dse}$, $R_{\rm dse}$, and R_{ie} are the elements of the design-oriented FET model, $R_0 = 50\ \Omega$

$$R_{io} = R_0 + R_{ie}$$
$$R_{\rm dso} = \frac{R_{\rm dse}R_0}{R_{\rm dse} + R_0}.$$

The expression of S_{11} for the design-oriented FET model is

$$S_{11} = \frac{\left(1 + j2\pi f\ (\text{GHz})C_{\rm gse}\ (\text{pF})(R_{ie} - R_0)10^{-3}\right)}{\left(1 + j2\pi f\ (\text{GHz})C_{\rm gse}\ (\text{pF})(R_{ie} + R_0)10^{-3}\right)}. \tag{8}$$

The circuit that better describes the FET S_{22} frequency behavior has the topology shown in Fig. 1(c). The analytical expression of the

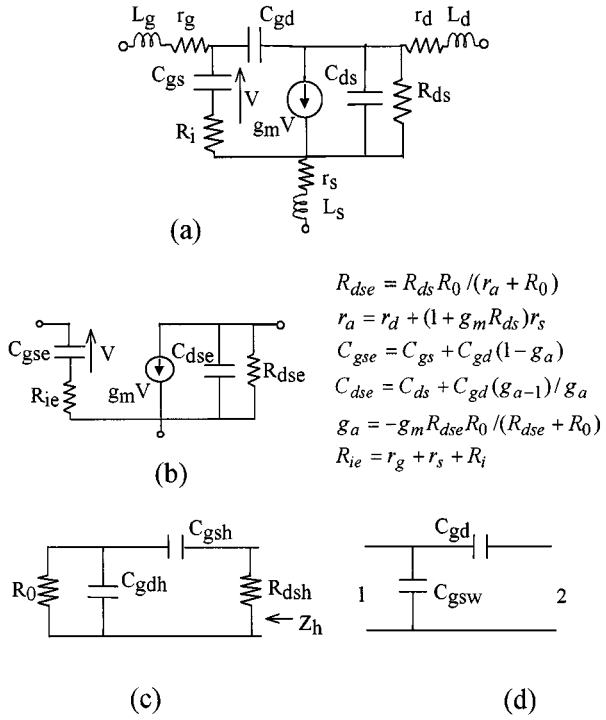

Fig. 1. (a) FET complete model. (b) Design-oriented FET model. (c) New simple circuit describing the FET S_{22}. (d) New simple circuit describing the FET S_{12}.

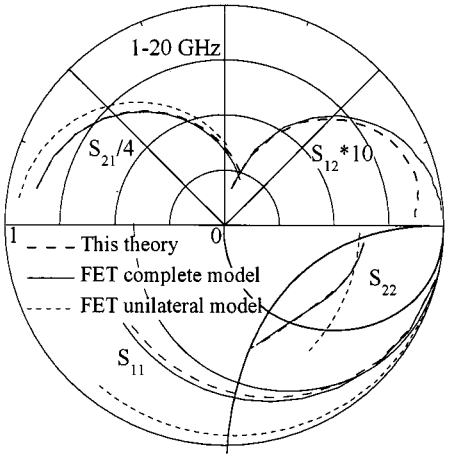

Fig. 2. S-parameters of typical 0.5-μm gate-length MESFET.

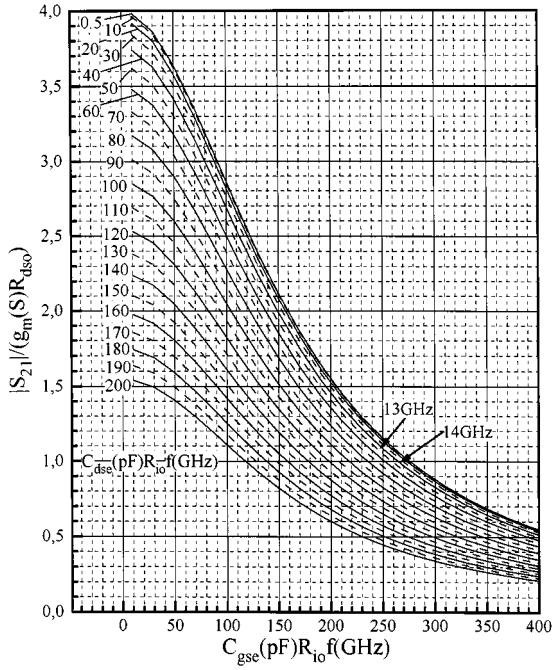

Fig. 3. Chart to derive the term $|S_{21}|/g_m(S)R_{\rm dso}$ as a function of $C_{\rm gsc}$ (pF)$R_{io}f$ (GHz) with $C_{\rm dsc}$ (pF)$R_{\rm dso}f$ (GHz) as the parameter.

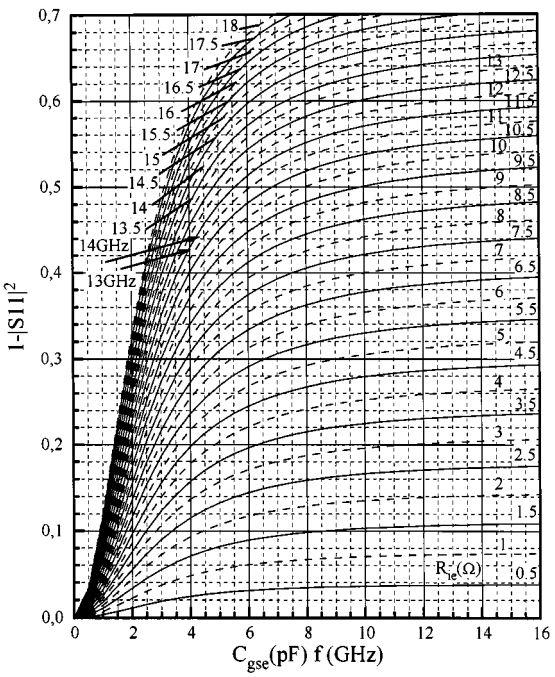

Fig. 4. Chart to derive the term $1-|S_{11}|^2$ as a function of $C_{\rm gse}$ (pF)f (GHz) with R_{ie} as the parameter.

impedance Z_h of this simple circuit and the FET complete model output impedance were compared. The output impedance of the FET was calculated neglecting r_s, r_g, r_d, and R_i in the complete model. After some algebraic manipulation, the new simplified expression of S_{22} is (9), shown at the bottom of this page, where

$$C_{\rm gdh}\ ({\rm pF}) = C_{\rm gd}\ ({\rm pF})\Big(1 + g_m(S)R_0 + C_{\rm ds}\ ({\rm pF})/C_{\rm gd}\ ({\rm pF})\Big)$$
$$C_{\rm gsh}\ ({\rm pF}) = C_{\rm gdh}\ ({\rm pF}).$$

$R_{\rm dsh} = r_s + r_d + R_{\rm ds}(1 + g_m r_s)$. $R_{\rm dsh}$ is the output resistance of the FET complete model calculated assuming low-frequency conditions.

The same method was used to obtain a simple expression of S_{12}. The circuit chosen to derive the S_{12} of the FET is shown in Fig. 1(d). The S_{12} of the FET complete model was calculated neglecting r_s, r_g, r_d, and R_i. Comparing the expression for S_{12} of the circuits in Fig. 1(d) and of the FET complete model [see Fig. 1(a)], after some simplifications, the approximate expression of S_{12} is (10), shown at the bottom of this page, where

$$C_{\rm gsw}\ ({\rm pF}) = C_{\rm gd}\ ({\rm pF})R_0\Big(g_m(S) + 1/R_{\rm ds}\Big) + C_{\rm gs}\ ({\rm pF})(1 + R_0/R_{\rm ds}) + C_{\rm ds}\ ({\rm pF}).$$

In all the cases, the parasitic inductances L_g, L_d, and L_s were neglected. L_g and L_d are normally absorbed in the matching networks. L_s affects the accuracy of the results, but can be neglected without significant error.

The validity of the new expressions of the S-parameters is demonstrated by comparing the S-parameters derived from the FET complete model (typically extracted from measurements). L_g and L_d were not included in the FET complete model.

$$S_{21} = \frac{2g_m(S)R_{\rm dso}}{\Big(1 + j2\pi f\ ({\rm GHz})C_{\rm gse}\ ({\rm pF})R_{io}10^{-3}\Big)\Big(1 + j2\pi f\ ({\rm GHz})C_{\rm dse}\ ({\rm pF})R_{\rm dso}10^{-3}\Big)} \tag{7}$$

$$S_{22} = \frac{\Big(1 + j4\pi f\ ({\rm GHz})C_{\rm gd}\ ({\rm pF})R_0 10^{-3}\Big)R_{\rm dsh}}{1 + j2\pi f\ ({\rm GHz})C_{\rm gdh}\ ({\rm pF})(2R_0 + R_{\rm dsh})10^{-3} - \Big(2\pi f\ ({\rm GHz})C_{\rm gdh}\ ({\rm pF})10^{-3}\Big)^2 R_0 R_{\rm dsh}} \tag{9}$$

$$S_{12} = \frac{j2\pi f\ ({\rm GHz})C_{\rm gd}\ ({\rm pF})R_0 10^{-3}}{1 - \Big(2\pi f\ ({\rm GHz})R_0 10^{-3}\Big)^2 C_{\rm gsw}\ ({\rm pF})C_{\rm gd}\ ({\rm pF}) + j2\pi f\ ({\rm GHz})\Big(C_{\rm gsw}\ ({\rm pF}) + 2C_{\rm gd}\ ({\rm pF})\Big)10^{-3}R_0} \tag{10}$$

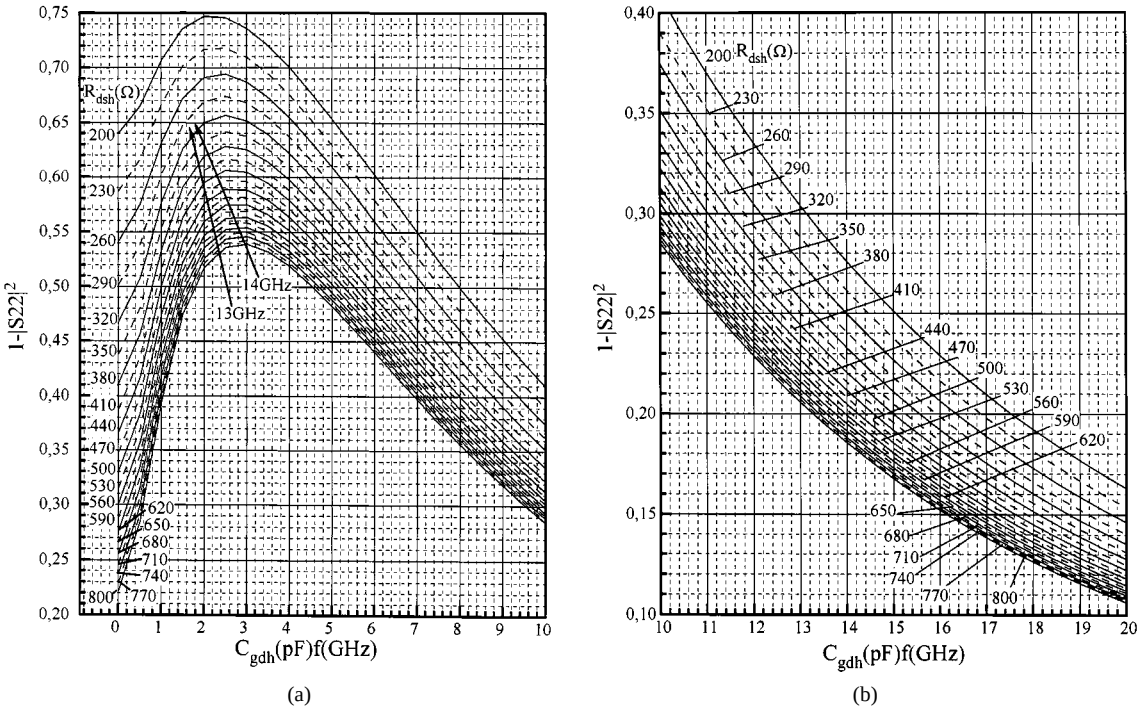

Fig. 5. Chart to derive the term $|S_{22}|$ as a function of $C_{\rm gdh}$ (pF)f (GHz) with $R_{\rm dsh}$ as the parameter.

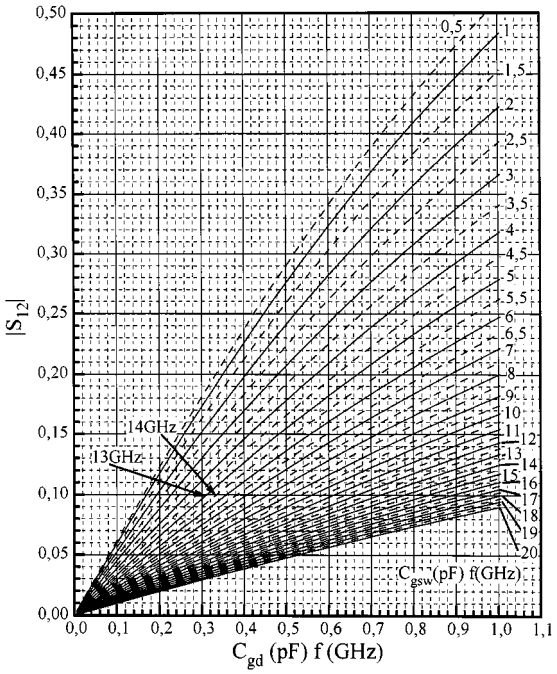

Fig. 6. Chart to derive the term $1-|S_{12}|^2$ as a function of $C_{\rm gd}$ (pF)f (GHz) with $C_{\rm gsw}$ (pF)f (GHz) as the parameter.

Fig. 2 shows the S-parameters for a typical 0.5-μm gate-length MESFET up to 20 GHz. As further comparison, the S-parameters derived from the FET unilateral model (same topology in Fig. 1(b) assuming $R_{\rm dse}=R_{\rm ds}$, $R_{ie}=R_i$, $C_{\rm gse}=C_{\rm gs}$, and $C_{\rm dse}=C_{\rm ds}$) are also shown. Good agreement, in amplitude and phase, is demonstrated.

Since the purpose of this paper is to provide a fast manner to compute the modules of the S-parameters for evaluating the different power gains, a graphic presentation is proposed. Four sets of curves are sufficient to calculate the S-parameter modules.

The term $|S_{21}|/g_m(S)R_{\rm dso}$ as a function of $C_{\rm gse}$ (pF)$R_{io}f$ (GHz) with $C_{\rm dse}$ (pF)$R_{\rm dso}f$ (GHz) as the parameter is plotted in Fig. 3. The term $1-|S_{11}|^2$ as a function of $C_{\rm gse}$ (pF)f (GHz) with R_{ie} as the parameter is plotted in Fig. 4. The term $1-|S_{22}|^2$ as a function of $C_{\rm gdh}$ (pF)f (GHz) with $R_{\rm dsh}$ as the parameter is plotted in Fig. 5(a) and (b). In this case, the figure is split to simplify the evaluation of the term $1-|S_{22}|^2$. Finally, the term $|S_{12}|$ as a function of $C_{\rm gd}$ (pF)f (GHz) with $C_{\rm gsw}$ (pF)f (GHz) as the parameter is plotted in Fig. 6. In Table I are listed all the terms necessary to calculate the modules of the S-parameters from the charts in Figs. 3–6.

The range of the parameters to plot Figs. 3–6 is chosen to permit the computation of S-parameter modules for typical MESFET's and high electron-mobility transistors (HEMT's). Furthermore, an approximate expression of the stability factor k is also given to calculate G_{ma} and to find the frequency that limits the FET instability zone

$$k=\frac{1-|S_{11}|^2-|S_{22}|^2+|S_{11}|^2|S_{22}|^2+|S_{12}|^2|S_{21}|^2}{2|S_{12}||S_{21}|}. \qquad (11)$$

Once the elements of the design-oriented FET model $C_{\rm gse}$, $C_{\rm dse}$, $R_{\rm dse}$, R_{ie}, and the terms in Table I are calculated, the modules of the S-parameters for the required frequency f are obtained from the charts in Figs. 3–6.

To show the effectiveness of this method, an example of amplifier design is described. The MESFET whose S-parameters are reported in Fig. 2 is used. The design goal is more than 18-dB gain in 13–14-GHz frequency band with -12 dB of return loss. The first step of the design is verifying the stability of the active device. If this condition is verified, then G_{ma} will be calculated. The transducer gain of the whole amplifier must be lower than the sum of G_{ma} (G_{ma} is equal to the maximum transducer gain) of each FET, calculated at the highest frequency of the band. This allows to evaluate the number of stages necessary to get the design goal. Table II(a) lists the values of the FET complete model elements. Table II(b) lists the values of the terms constant with frequency from Table I. In Table II(c), the calculated S-parameter modules at the

TABLE I
TERMS TO DERIVE THE S-PARAMETER MODULES FROM THE CHARTS IN FIGS. 3–6

$\lvert S_{21}\rvert$
$R_{io} = R_0 + R_{ie}$
$R_{dso} = \dfrac{R_{dse} R_0}{R_{dse} + R_0}$
$C_{gse}(pF) R_{io} f(GHz)$
$C_{dse}(pF) R_{dso} f(GHz)$
$\lvert S_{11}\rvert$
$C_{gse}(pF) f(GHz)$
$\lvert S_{22}\rvert$
$C_{gdh}(pF) = C_{gd}(pF)\left(1 + g_m(S) R_0 + \dfrac{C_{ds}(pF)}{C_{gd}(pF)}\right)$
$R_{dsh} = r_s + r_d + R_{ds}\left(1 + g_m(S) r_s\right)$
$C_{gdh}(pF) f(GHz)$
$\lvert S_{12}\rvert$
$C_{gsw}(pF) = C_{gd}(pF) R_0\left(g_m(S) + \dfrac{1}{R_{ds}}\right) + C_{gs}(pF)\left(1 + \dfrac{R_0}{R_{ds}}\right) + C_{ds}(pF)$
$C_{gd}(pF) f(GHz)$
$C_{gsw}(pF) f(GHz)$

TABLE II
EXAMPLE OF AMPLIFIER DESIGN

a) FET complete model elements

g_m (S)	C_{gs} (pF)	C_{gd}(pF)	C_{ds} (pF)	R_{ds}(Ω)	R_i(Ω)	r_g(Ω)	r_d(Ω)	r_s(Ω)
0.036	0.246	0.024	0.06	279.7	3.12	6.15	3.06	2.1

b) Design-oriented FET model elements and constant parameters (Table I)

R_{dse} (Ω)	R_{ie} (Ω)	C_{gse} (pF)	C_{dse} (pF)
182.9	11.39	0.31	0.99

C_{gse} (pF)	R_{io} (Ω)	C_{dse} (pF)	R_{dso} (Ω)	C_{gdh} (pF)	R_{dsh} (Ω)	C_{gsw} (pF)
18.97		3.88		0.127	306	0.4

c) MESFET S-parameters from this method

f (GHz)	|S11|	|S21|	|S12|	|S22|
13	0.757	1.46	0.098	0.597
14	0.745	1.38	0.099	0.591

d) Gains and k (The results for the FET complete model are in brackets)

f (GHz)	G_T (dB)	G_{ma} (dB)	G_{TUmax}(dB)	G(dB)	G_A(dB)	k
13	3.3	10.63	8.9	6.99	5.21	1.033
	(3.77)	(10.96)	(9.01)	(7.1)	(5.27)	(0.99)
14	2.77	9.25	8.16	6.29	4.64	1.126
	(3.3)	(9.42)	(8.26)	(6.39)	(4.7)	(1.07)

edges of the frequency band are shown (arrows in Figs. 3–6 indicate the corresponding values). Finally, in Table II(d), the various gains and stability factor calculated by the S-parameters in Table II(c) are listed.

The stability of the MESFET is assured as reported in Table II(d). A $G_{ma} = 9.25$ dB at 14 GHz is obtained. A two-stage amplifier can theoretically provide a transducer gain of about 18.5 dB in the whole frequency band. The simulation of the circuit using Touchstone shows a gain of 19±0.3 dB. In particular, a gain of 18.7 dB at 14 GHz results, very close to the value predicted by this method.

III. CONCLUSION

A set of new, simple, and accurate expressions for computing FET S-parameters as a function of the circuit elements of the FET complete model has been presented in this paper. The fast calculation of the S-parameter modules by four charts permits straightforward evaluation of the main definitions of FET power gain. The accuracy of this simplified procedure was demonstrated by comparisons with the results from simulation of the FET complete model. This method permits the designer to evaluate the FET performance by using only a pocket calculator.

REFERENCES

[1] G. D. Vendelin, *Design of Amplifiers and Oscillators by the S-Parameter Method*. New York: Wiley, 1982.
[2] C. Paoloni and S. D'Agostino, "An approach to distributed amplifier based on a design-oriented FET model," *IEEE Trans. Microwave Theory Tech.*, vol. 43, pp. 272–277, Feb. 1995.

Dual-Mode Helical Resonators

R. S. Kwok and S. J. Fiedziuszko

***Abstract*—High performance and compact size are the most important criteria in filter-based products for satellite communication systems. Succeeding the superconducting and dielectric resonators, the conventional single-mode helical resonator ranks favorably on its high unloaded-Q per volume. Improvement of the performance has been demonstrated by operating the helical resonator at a higher order ($n > 0$) mode. In addition, these resonators can also be fabricated onto a high dielectric-constant material to further reduce the size of the filter structure. Detailed design considerations of the dual-mode wire-wound helical resonator filter, as well as implementation of the dual-mode dielectrically loaded helical resonator filter structure, are presented in this paper.**

I. INTRODUCTION

Helical filters have been used extensively in RF and low microwave frequencies in which the conventional lumped-element filters are too lossy and the quarter-wave coaxial resonators are too large. These helices are designed to operate in their cylindrically symmetric fundamental mode ($n = 0$). Details of such technology have been reviewed by a number of authors [1]–[3]. To further reduce the size of the single-mode helical filters, dielectric-loaded helices have recently been introduced [4]. At the same time, a higher order dual-mode helical filter was also proposed. Design of this higher order helical resonator is very complicated and not yet fully understood, mainly because of the absence of an analytical solution. In this paper, we present the design concept, the approximation used, and the experimental realization of a half-wavelength dual-mode helix loaded cavity filter. Similar to the single-mode resonators, the dual-mode helices can also be fabricated onto a high dielectric-constant material. Results of these newly developed dual-mode dielectric-loaded helical resonators will also be discussed.

Manuscript received October 19, 1998; revised December 10, 1999.
The authors are with Space Systems/LORAL, Palo Alto, CA 94303 USA (e-mail: kwok.raymond@ssd.loral.com).
Publisher Item Identifier S 0018-9480(00)02062-7.

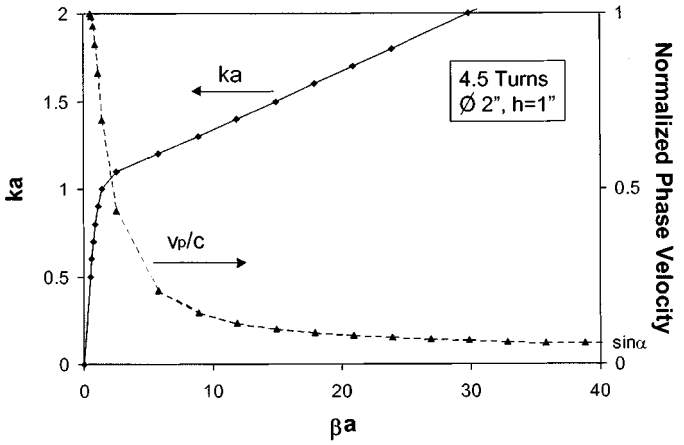

Fig. 1. Dispersion relation and phase velocity of a sheath helix operating at $n = 1$ mode.

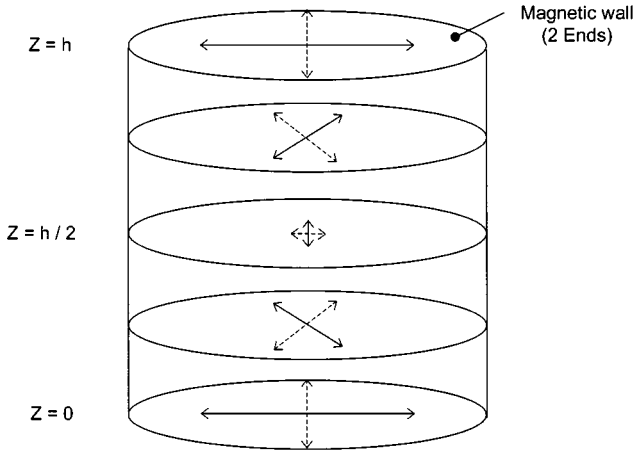

Fig. 2. Oscillating electric-field pattern for the two orthogonal modes of an $n = 1$ half-wave helical resonator.

II. Sheath Model

The sheath model is a popular mathematical description of a helix because of its simplicity and ability to account for many helical properties. A sheath helix is basically a cylindrical tube assumed to have infinite conductivity in the direction of the original helical winding and zero conductivity in a direction normal to the turns of the winding. Excellent literature on the sheath model [5]–[8] are readily available, including a detailed 1995 review by Sensiper.

Following the derivations outlined by Collin [5] and Sensiper [6] for an nth-order sheath helix, one would obtain a transcendental eigenvalue equation

$$\frac{K_n'(ha)I_n'(ha)}{K_n(ha)I_n(ha)} = -\frac{(h^2a^2 + n\beta a\cot\alpha)^2}{K_o^2 a^2 h^2 a^2 \cot^2\alpha} \tag{1}$$

where k_o is the free-space phase constant $(=\omega/c)$, β is the axial phase constant $(=\omega/v)$, v is the phase velocity of the wave, h is the radial phase constant defined by $\beta^2 = h^2 + k_o^2$, α is the pitch angle, I_n and K_n are the modified Bessel functions of order n, and the primes are the derivative of the Bessel functions with respect to the argument ha. The guided wavelength can then be approximated by numerically solving this eigenvalue equation. Similar to the dielectric resonator, the lowest order eigenstate of a helical resonator that displays the duality nature

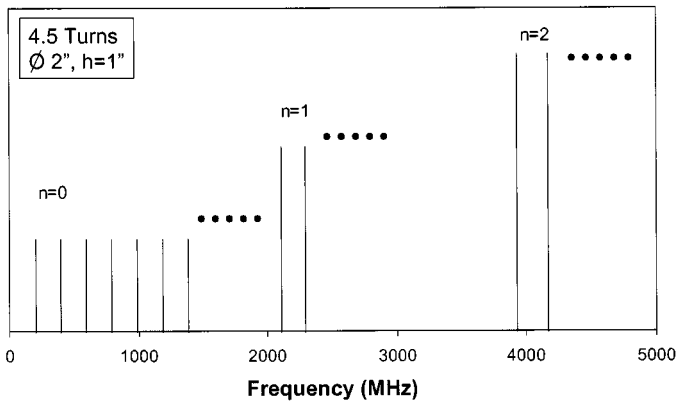

Fig. 3. Spectrum for $n = 0$, 1, and 2 modes of a helical resonator approximated by the sheath model.

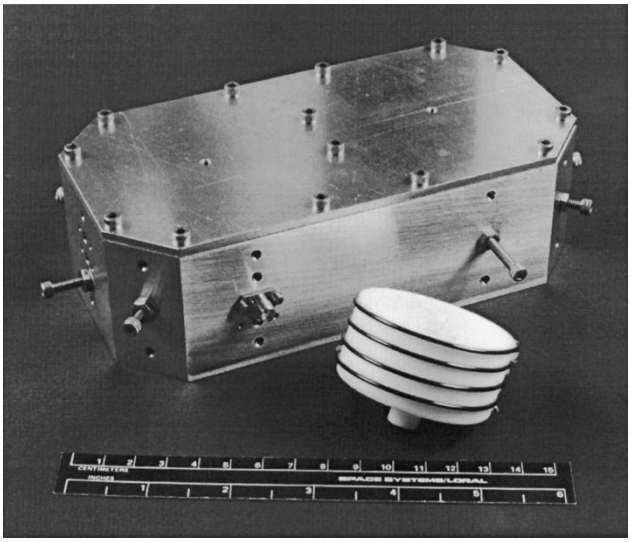

Fig. 4. Dual-mode helical resonator loaded cavity filter (copper helix on Teflon core in bare aluminum cavities).

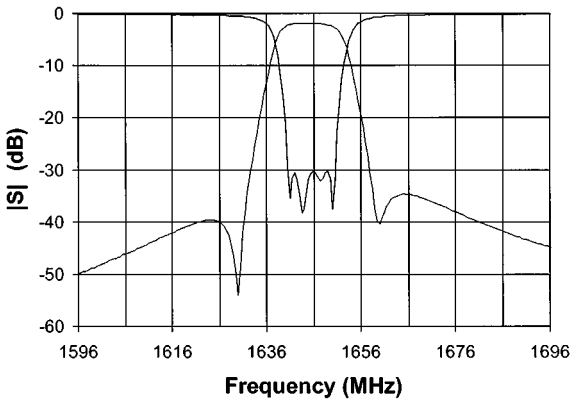

Fig. 5. Measured quasi-elliptical response of a dual-mode helical resonator loaded cavity filter (four pole 10-MHz bandwidth, 1.8-dB insertion loss, realized unloaded Q of 1400).

of the electromagnetic-field pattern is the $n = 1$ mode, even though the field distributions of the two cases are quite different.

For a helix of 4.5 turns, 2-in diameter, and 1-in height, (1) has been solved numerically for the case of $n = 0, 1$, and 2. The resulted dispersion relation and the phase velocity for $n = 1$ mode (shown in Fig. 1)

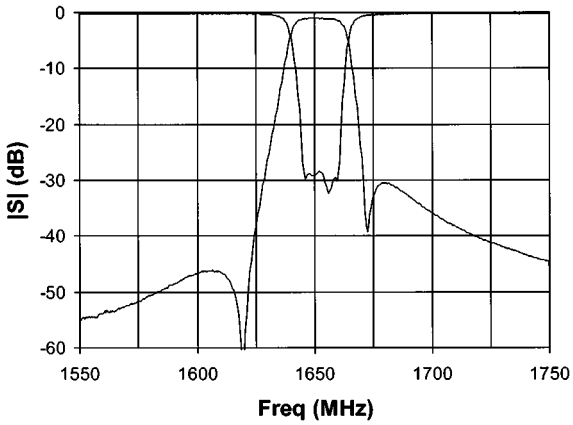

Fig. 6. Measured response of the same filter in Fig. 4 with silver-plated elements and new coupling probes (quasi-elliptical response, 15-MHz bandwidth, 0.96-dB insertion loss, realized unloaded Q of 1800).

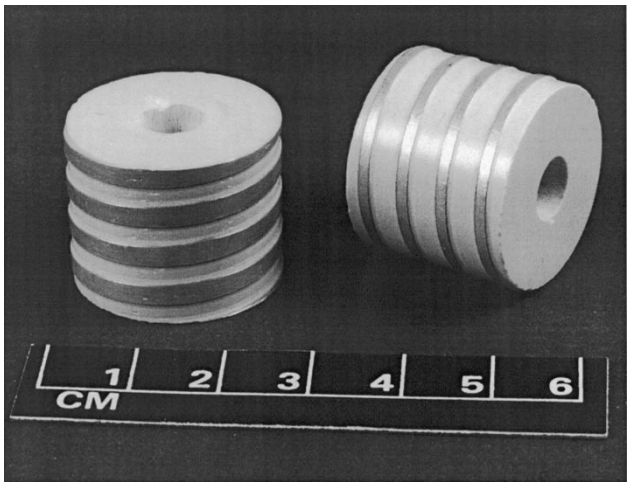

Fig. 7. Helical patterns fabricated onto dielectric resonators of 1-in diameter and 0.8-in height.

is similar to those of the fundamental mode [5]–[8]. For large $k_o a$, the wave can be thought of as spiraling along the helix and, consequently, the phase velocity is reduced by the geometric factor of $\sin\alpha$.

The corresponding field distributions obtained is similar to that of the HE_{11} hybrid mode of a dielectric resonator with the following noticeable differences.

1) The field intensity is mostly concentrated around the circumference and is minimal at the center.
2) The field direction spiral along the helix.
3) The radial electric field inside and outside of the helix are opposite in direction.

By imposing a reflective boundary at each of the two ends, a spiral standing wave is formed as illustrated in Fig. 2 for the case of using perfect magnetic walls. One can see that two independent sets of solutions exist (solid and dashed lines) in Fig. 2 corresponding to the two orthogonal modes. Depending on how the boundaries are physically implemented, electric walls can also be used provided a 180° phase shift is included upon reflection. Nevertheless, the following discussions apply to either condition.

Finally, spectrum of the nth-order helical resonator mode can be approximated by equating L to an integer multiple of $\lambda_g/2$. The estimated resonant frequencies of the sheath helix for $n = 0$, 1, and 2 modes are shown in Fig. 3. The fundamental spectrum ($n = 0$) is similar to those recently reported [9], in which the frequency-dependent transverse impedance was explicitly taken into account. Utilizing this result, dual-mode helical resonators were discovered. Cavity filters loaded with such resonators were built and tested. Details of the experiment are described in the following section.

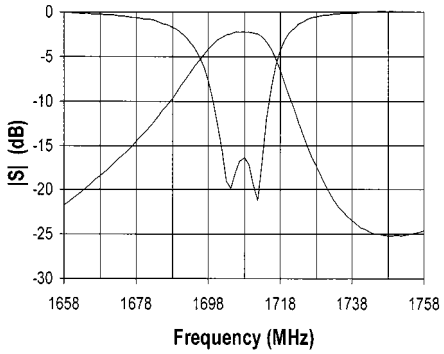

Fig. 8. Measured response of the dual-mode dielectric loaded helical resonator in Fig. 7 (single resonator, 12-MHz bandwidth, 2.2-dB insertion loss, realized unloaded Q of 500).

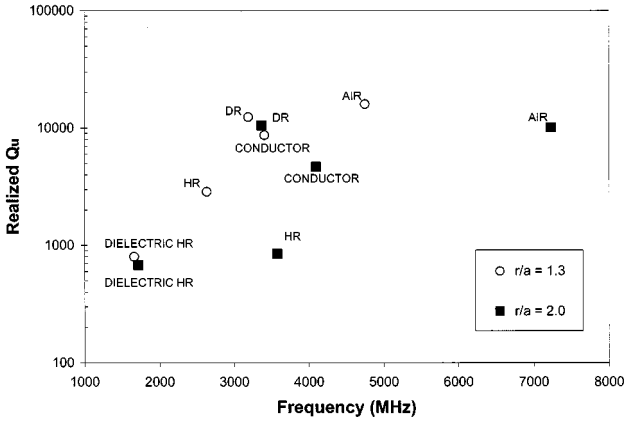

Fig. 9. Realized unloaded Q of the dual-mode cavity resonators with various loading (open circles: $r/a = 1.3$, solid squares: $r/a = 2.0$).

III. Dual-Mode Helical Resonator Loaded Cavity Filters

The helical resonators used for the dual-mode filters (Fig. 4) and its measured response of a four-pole Chebyshev filter was previously reported [4]. The quasi-elliptical response of the modified filter is shown in Fig. 5. The center frequency of the filter is around 1.65 GHz, which is somewhat lower than the 2 GHz estimated from the spectrum in Fig. 3. This is due to the oversimplification of our model, in which neither the loading of the cavity, dielectric holder, and coupling mechanism nor the fringing effects are taken into account. The realized unloaded Q of the filter is measured to be 1400. When silver-plated housing, wire, and tuning screws are used, the realized unloaded Q factor is enhanced to 1800 (see Fig. 6).

Fig. 3 suggests that there are many spurious around the desired frequency, which was observed in a dual-mode resonator. However, with an increased number of resonators, most of the spurious are suppressed. Furthermore, helices with different geometry can be mixed together in a way that the unwanted resonant frequencies of each helix are not co-located. Altogether, the spurious can be managed to an acceptable level.

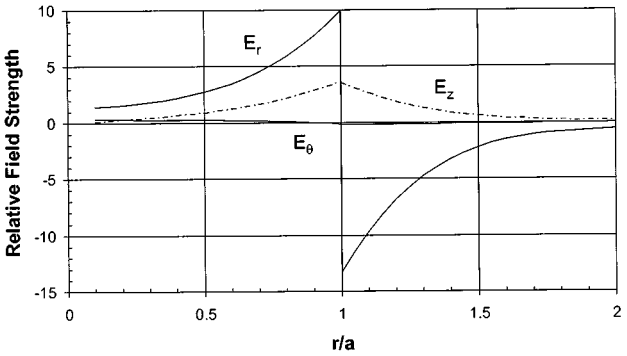

Fig. 10. Maximum strength of the unperturbed electric field components of a $n = 1$-mode sheath helix.

IV. Dual-Mode Dielectric Loaded Helical Resonators

To further reduce the size of the helical resonator, we fabricated helical patterns onto dielectric resonators, as demonstrated in Fig. 7. This can be achieved by using chemical or laser etching, thick silver painting, or electroplating processes. A dielectric resonator of $\varepsilon_r = 20$, 1-in diameter, and 0.8-in height, with four turns of metallic strip was placed inside a cavity of 1.3-in diameter. The first detectable dual-mode resonant is at 1.7 GHz. The realized unloaded Q is about 500–680, as shown in Fig. 8. For a comparison, various types of dual-mode resonators [10]–[13] with the same overall dimensions were measured in the same cavity and the realized unloaded Q are displayed as open circles in Fig. 9. Although this might not be the best way to compare the different technologies because the Q_u is also a function of frequency, it does provide a good reference and is certainly the most economical method. The empty cavity and dielectric resonator loaded cavity have a Q_u of over 10 000. The conductor-loaded cavity is about half of that, and for a four-turn wire-wound helix of 1-in inside diameter, a Q_u of 850 is obtained, which is much too low for that frequency.

In reviewing the electric-field intensity of the sheath model (Fig. 10), we realized that the first filter built has a r/a ratio of 1.6 and a Q_u of 1800. This smaller helix has a ratio of $r/a = 1.3$, where the unperturbed electric field is still quite substantial and, consequently, the Q_u is much lower $(=850)$. Fig. 10 then implied that the cavity should be chosen such that r/a is almost equal to or greater than two. The above experiment was repeated with a larger cavity of 2-in diameter (denoted as solid squares in Fig. 9). The Q_u of the same wire-wound helix was increased to 2880. Note that both the air cavity and conductor-loaded cavity had improved their Q_u to 16000 and 8700, respectively, while the dielectric resonator and dielectric loaded helix varied only slightly in Q_u and resonant frequency because the electric field is mostly concentrated inside the dielectric. Since the Q_u is not limited by the $\tan\delta$ of the dielectric, one could, in principle, use a higher dielectric constant and a smaller cavity to significantly further reduce the size of the helical resonator.

The Q_u of the resonators reported here are not optimized to their full potential. The realized Q_u is measured by the filter response, which includes all the losses from the structure and coupling mechanisms. With an increased coupling, the measured Q_u can be reduced substantially. The helical resonators under study required very strong coupling, which, in turn, limited the Q_u. Different coupling mechanisms should be investigated to maximize the available Q_u of these filter structures.

V. Conclusion

Novel configurations for dual-mode wire-wound and dielectric loaded helical resonator filters have been demonstrated. Excellent experimental results have been obtained in this initial work and substantial improvement is expected. However, significant theoretical work needs to be completed to explore the full potential of the helix structures.

To include the helical symmetry explicitly in our approximations, a tape model [6], [7] was also considered. A periodic dispersion relation was resulted from this periodicity imposed. Nonetheless, our preliminary study indicated that this model does not offer more critical information than the simpler sheath model. Full-wave analyses of more precise representations are needed to fully understand the observed properties such as the helix-orientation dependence of the measurement. Much of the helical resonator characteristics are still not well understood; this opens a new area for theoretical and experimental investigation of these very promising microwave structures.

Acknowledgment

The authors acknowledge PicoFarad, Anaheim, CA, for providing the dielectric resonators used in these experiments.

References

[1] A. I. Zverev, *Handbook of Filter Synthesis*. New York: Wiley, 1976, ch. 9.
[2] P. Vizmuller, *Filters with Helical and Folded Helical Resonators*. Norwood, MA: Artech House, 1987.
[3] W. W. Macalpine and R. O. Schildknecht, "Coaxial resonators with helical inner conductor," *Proc. IRE*, pp. 2099–2105, 1959.
[4] S. J. Fiedziuszko and R. S. Kwok, "Novel helical resonator filter structures," in *IEEE MTT-S Int. Microwave Symp. Dig.*, Baltimore, MD, 1998, pp. 1323–1326.
[5] R. E. Collin, *Field Theory of Guided Waves*. New York: McGraw-Hill, 1960, pp. 637–640.
[6] S. Sensiper, "Electromagnetic wave propagation on helical structures," *Proc. IRE*, pp. 149–161, 1955.
[7] R. E. Collin, *Foundations of Microwave Engineering*. New York: McGraw-Hill, 1966, pp. 580–585.
[8] J. R. Pierce, *Traveling Wave Tubes*. New York: Van Nostrand, 1950.
[9] J. A. Mezak, "Modeling helical air coils for wireless and RF applications," *R.F. Des.*, pp. 77–79, Jan. 1998.
[10] A. E. Atia and A. E. Williams, "Narrow bandpass waveguide filters," *IEEE Trans. Microwave Theory Tech.*, vol. MTT-20, pp. 258–265, Apr. 1972.
[11] S. J. Fiedziuszko, "Dual mode dielectric resonator loaded cavity filters," *IEEE Trans. Microwave Theory Tech.*, vol. MTT-30, pp. 1311–1316, Sept. 1982.
[12] S. J. Fiedziuszko and J. A. Curtis, "Plural-mode stacked resonator filter including superconductive material resonators," U.S. Patent 5 484 764, Jan. 16, 1996.
[13] C. Wang, K. A. Zaki, and A. E. Atia, "Dual-mode conductor-loaded cavity filters," *IEEE Trans. Microwave Theory Tech.*, vol. 45, pp. 1240–1246, Aug. 1997.